INL/JOU-24-76220-Revision-0

Impact of anisotropy on TRISO fuel performance

December 2024

Gyanender Singh, Jordan Andrew Evans, Wen Jiang, Jason D Hales, Stephen R Novascone

Changing the World's Energy Future

Idaho National Laboratory

INL/JOU-24-76220-Revision-0

Impact of anisotropy on TRISO fuel performance

Gyanender Singh, Jordan Andrew Evans, Wen Jiang, Jason D Hales, Stephen R Novascone

December 2024

Idaho National Laboratory
Idaho Falls, Idaho 83415

http://www.inl.gov

Prepared for the
U.S. Department of Energy
Under DOE Idaho Operations Office
Contract DE-AC07-05ID14517

Impact of Anisotropy on TRISO Fuel Performance

Gyanender Singh[a,*], Jordan A. Evans[b], Wen Jiang[a], Jason Hales[a], Stephen Novascone[a]

[a] *Idaho National Laboratory, Computational Mechanics and Materials, P.O. Box 1625, Idaho Falls, ID 83415*
[b] *Idaho National Laboratory, Irradiated Fuels and Materials, P.O. Box 1625, Idaho Falls, ID 83415*

Abstract

Manufacturing of tristructural isotropic (TRISO) particles involves the deposition of pyrolytic carbon (PyC) and silicon carbide (SiC) layers using the fluidized bed chemical vapor deposition (CVD) process. The CVD process is known to generate polycrystalline layers with crystallographic textures, which imparts anisotropic thermophysical properties to the layers. Past studies have shown the risk for particle failure increases with an increase in anisotropy. The limit beyond which the anisotropy of PyC layers becomes unacceptable due to failure risk has been identified as a high-priority knowledge gap. This work presents a first systematic study on the effects of anisotropic thermal and mechanical properties on TRISO fuel performance. This computational study, performed using the fuel performance code BISON, investigates how the anisotropy in elasticity and thermal properties affect the stresses, temperature, and failure of a TRISO particle. The influence of other factors, such as operating temperature and particle geometry on the anisotropy effects, also has been analyzed. The studies utilize the recently published anisotropic elasticity and thermal behavior models for TRISO PyC and SiC layers implemented using tensors with full anisotropic capability. The spherical TRISO particles with anisotropic properties were found to have greater maximum tensile stress and significantly higher failure probability than the spherical particles with isotropic properties. The fuel performance predicted using these recently developed models was found to be comparable with the performance obtained using the historical models.

Keywords: TRISO, HTGR, BISON, anisotropy, fuel performance, modeling

1. Introduction

Tristructural isotropic (TRISO) nuclear fuel is a ceramic nuclear fuel candidate applicable for several next-generation nuclear power designs, including gas-cooled reactors, molten salt-cooled reactors, and liquid metal-cooled microreactors. The general design of the TRISO particle involves a fuel kernel—typically uranium oxycarbide (UCO) or uranium dioxide (UO_2)—surrounded by several protective coating layers, as shown in Figure 1. TRISO fuel is expected to be robust and resistant to the extreme temperatures, pressures, and radiation fields associated with next-generation nuclear reactor designs. The primary emphasis regarding the performance of a TRISO fuel particle is on

[*] corresponding author
Email address: gyanender.singh@inl.gov (Gyanender Singh)

maintaining the structural integrity of the particle at normal—as well as accident—conditions to minimize the release of the fission products. The secondary emphasis is on attaining high-burnup to allow economic operation and efficient utilization of the fissile material [1].

Combining the thermomechanical properties of TRISO fuel with known reactor conditions (neutron flux, temperatures, pressures, etc.) allows the simulation of TRISO nuclear fuel performance. A Monte Carlo computational method can be utilized to simulate TRISO fuel failure probabilities under these conditions. TRISO fuel is generally treated as having isotropic thermomechanical properties (hence the name "tristructural isotropic") in fuel performance simulations [2]. The buffer and SiC layers are always assumed to be isotropic in historical models, and texture is accounted for in the PyC layers only in historical TRISO fuel performance models via the bacon anisotropy factor (BAF) see for example [3]), which homogenizes the properties into scalar (isotropic) values. Fluidized bed chemical vapor deposition (CVD) is used to deposit the carbon and silicon carbide (SiC) coatings of TRISO particles [4–7]. CVD is a technology that is known to result in fine-grained polycrystalline structures with potentially large crystallographic textures [6, 8–11]. Modern characterization methods, such as two-modulator generalized ellipsometer (2-MGE) measurements [12–14], electron backscatter diffraction (EBSD) [15, 16], transmission electron microscopy (TEM) [10, 11, 17–19], and Raman spectroscopy [19, 20], have confirmed the as-fabricated coatings of TRISO particles—especially the carbon coatings have small texture - see references [21–23] for details of the fabricated fuel. There is lack of measurements for texture evolution in the irradiated TRISO fuel, however, the ion beam studies suggest that the texture of the PyC layers increases further with increasing radiation damage [24, 25].

The SiC layer is the primary structural layer and pressure vessel of the TRISO particle. In general, a TRISO particle is considered to have failed if the SiC layer is cracked. The thermophysical conditions that the SiC layer experiences are also dependent upon the properties and conditions of the surrounding carbon layers. In other words, it must be demonstrated that the anisotropic properties of the surrounding layers do not lead to a significant increase in the SiC failure probabilities. The limit beyond which the anisotropy of the PyC layers becomes unacceptable due to failure risk has been identified as a high-priority knowledge gap [26–28]. Evans et al. [29] recently calculated the texture-induced anisotropic thermomechanical properties of the TRISO particle layers based on experimental texture measurements and single crystal thermomechanical properties. In this work, the full elastic tensors of the transversely isotropic buffer, pyrolytic carbon (PyC), and silicon carbide (SiC) layers of a TRISO particle were calculated as a function of temperature for two symmetries: (1) isotropic, and (2) transversely isotropic. The calculated values were found to be in good agreement with those obtained using existing models at room temperature and correct orientation. The authors also calculated the temperature-dependent radial and tangential thermal conductivity of the TRISO layers using the Grüneisen-Debye theory. The ability to account for anisotropic thermomechanical properties of TRISO layers has been implemented in the BISON code [30].

The objective of this paper is to incorporate the recently calculated anisotropic thermomechanical properties of TRISO fuel into the newly developed anisotropic BISON framework under realistic advanced nuclear reactor conditions to evaluate the sensitivity of TRISO fuel failure to the texture-induced anisotropy of its constituent coating layers.

Additionally, BISON simulations are also performed to compute failure probabilities using the historical relationships as well in order to highlight differences in fuel performance when considering anisotropic TRISO coatings. This work also investigates the effect of temperature and geometry (spherical versus aspherical) on the failure probability of an anisotropic TRISO particle.

2. Methods

The performance of a TRISO particle was analyzed using the BISON code [31]. BISON is finite element-based nuclear fuel performance code applicable to a wide variety of fuel forms, such as light water reactor fuel rods, TRISO particle fuel, metallic rods, and plate fuel.

2.1. *Geometry Mesh and Fuel Irradiation Cases*

In this study, spherical particles were analyzed for understanding the effect of anisotropy; the effect of asphericity is separately presented in Section 4.5. The dimensions of the particle and its constituent layers are shown in Table 1. These dimensions are representative of the fuel particles used in the Advanced Gas Reactor (AGR)-2 experiment [32, 33]. The mesh of a particle is shown in Figure 1. The fuel kernel is surrounded by the carbon buffer layer, the inner pyrolytic carbon (IPyC) layer, the SiC layer, and the outer pyrolytic carbon (OPyC) layer in that order, radially outward. Each of the buffer, PyC, and SiC layers have eight elements in the radial direction and 60 elements in the circumferential direction. This mesh density is selected to achieve a converged solution.

Table 1. TRISO particle geometry

Fuel kernel radius	212.5 μm
Buffer thickness	100 μm
IPyC thickness	40 μm
SiC thickness	35 μm
OPyC thickness	40 μm

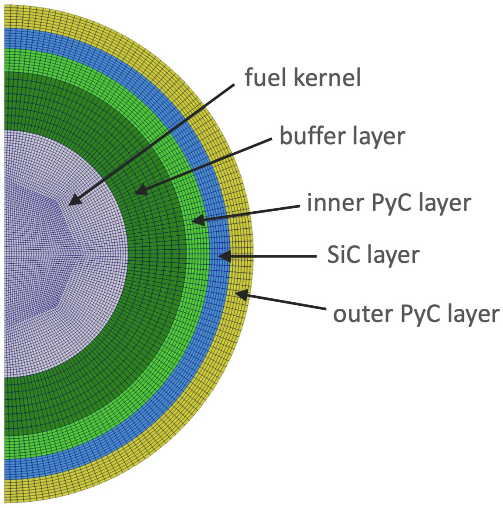

Figure 1. 2D axisymmetric meshed model of a spherical TRISO particle.

Three cases of fuel irradiation conditions were considered in the analysis with each case differing from other cases in terms of fuel temperature. These conditions are representative of AGR-2 experiment. The temperature conditions of each case are controlled by setting the temperature of the outer surface of the OPyC layer to a fixed value: (1) 1073K, (2) 1273K, and (3) 1473K. The temperatures were chosen so as to fall within the validity range of the material properties models. The details of the fuel irradiation conditions are listed in Table 2. The results presented are for the case with the temperature boundary condition of 1273K, unless otherwise stated.

Table 2. Fuel irradiation cases considered in the analysis

	Cases		
	1	2	3
Effective full power days (EFPD)	559	559	559
Burnup (%FIMA)	15	15	15
Fast fluence ($\times 10^{25}$ n/m^2, E >0.18 MeV)	5.6	5.6	5.6
Temperature at OPyC outer surface	1073K	1273K	1473K

2.2. *Fuel Kernel Properties*

The fuel is considered to be UCO which is more suitable for higher power density cores and higher burnup (> 20% FIMA) as compared to UO_2 (~11% FIMA) [34]. Table 3 list the properties of the fuel kernel assumed in this work.

Table 3. TRISO fuel properties

^{235}U enrichment (wt%)	15.5
Carbon/uranium (atomic ratio)	0.4
Oxygen/uranium (atomic ratio)	1.5
Kernel density (g/cm^3)	11.0
Kernel theoretical density (g/cm^3)	11.4
Buffer density (g/cm^3)	1.05
Buffer theoretical density (g/cm^3)	2.25
IPyC density (g/cm^3)	1.90
OPyC density (g/cm^3)	1.90

Further details of the UCO properties used in this analysis can be found in [35].

2.3. *Fuel Coating Properties*

2.3.1. *Elasticity Properties of TRISO Coating Layers*

The elasticity constants (C_{ij}) for the TRISO particle are based on Evans. et al. [29] and are considered to be dependent on the temperature, neutron fluence, and density. The expression for the elasticity constants is given in Eq. 1. These elasticity constants are representative of textures that are notably stronger than those observed in modern as-fabricated fuel (i.e., stronger than those measured in the AGR experiments [36]). The texture is generally quantified through the BAF, orientation angle (OA) or multiples of random distribution (MRD), depending on the method of measurement. The textures used in the analysis represent the two extremes – zero texture resulting in isotropy, and strong texture leading to significant anisotropy.

$$C_{ij}\ (\text{GPa}) = \begin{cases} A\left[1 + B(T-20)\right]\ (1+0.23\gamma)\,(0.384 + 0.324\times 10^{-3}\rho) & \text{for PyC and buffer} \\ A(1-6.0\epsilon_{irrad}^{vol}) & \text{for SiC} \end{cases} \tag{1}$$

where A and B are constants, T is temperature (°C), γ is the neutron fluence (x10^{25} n/m^2, E>0.18 MeV), ρ is the density (kg/m^3), and ϵ_{irrad}^{vol} is the irradiation-induced volumetric swelling strain. The values of A and B for each elasticity constant for the TRISO layers are listed in Table 4.

Table 4. Elasticity constant parameters for Evans model (reference: [29] and errata to [29])

	Elasticity constant	Buffer		PyC		SiC
		A	B	A	B	A
Anisotropy	C_{11}	3.15	0.00032	19.8	0.00032	490
	C_{22}	6.17	0.00032	38.8	0.00032	458
	C_{12}	0.19	0.00045	15.1	0.00045	71
	C_{23}	0.24	0.00045	19.4	0.00045	104
	C_{55}	0.86	0.000125	2.2	0.000125	148
Isotropy	C_{11}	4.11	0.00032	25.8	0.00032	438
	C_{12}	0.19	0.00045	15.5	0.00045	97

The variation of Young's moduli (E), shear moduli (G) and Poisson's ratios (ν) for the buffer, pyrolytic carbon (PyC), and SiC layers of the TRISO particle with temperature are shown in Figure 2 and Figure 3, respectively. The subscript p refers to in-plane direction, r refers to radial direction and iso refers to isotropic. For the PyC layers, texture with an orientation angle of 20° was considered, and a maximum texture for the SiC layer having a multiple of random distribution (MRD) of 10 was assumed [29]. These particular textures were selected because their corresponding full elastic tensors were determined previously. Note that these textures are not representative of the textures of the particles studied in the AGR program [21–23]. The case with isotropic properties is considered for comparison and based on reference [29].

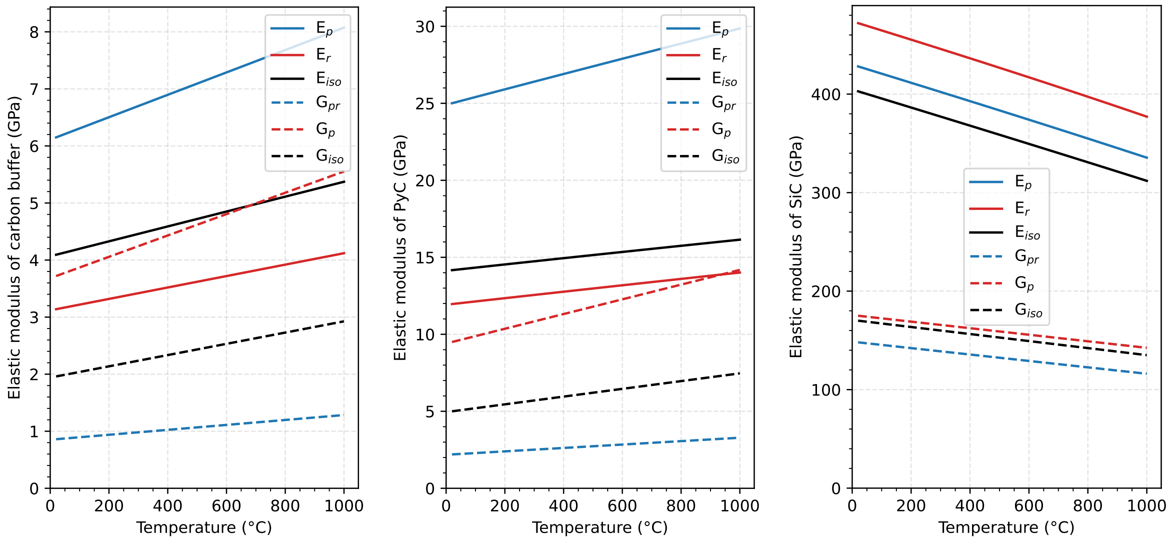

Figure 2. Elastic properties of the buffer, PyC, and SiC coating layers in a TRISO particle as a function of temperature assumed in this work, from [29].

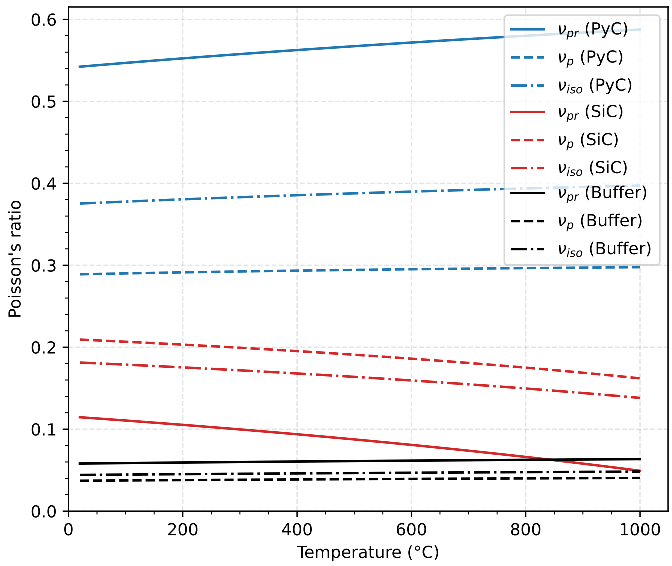

Figure 3. Poisson's ratio of the buffer, PyC, and SiC coating layers in a TRISO particle as a function of temperature [29].

The legacy models used for the elasticity properties are provided in the appendix.

2.3.2. *Thermal Properties of TRISO Coating Layers*

The expression for anisotropic thermal conductivity (radial and tangential components) and isotropic thermal conductivity based on Evans model [29] is given in Eq. 2.

$$k_{layer}^{component} = A_1T^6 + A_2T^5 + A_3T^4 + A_4T^3 + A_5T^2 + A_6T + A_7 \tag{2}$$

where A_i are constants and T is temperature (°C). The value of the constants are given in Table 5. Figure 4 presents the thermal conductivity of these constituent layers in the circumferential and radial direction. Note that these constituent layers have a transversely isotropic texture [37, 38]; they have the same properties in all directions perpendicular to the radial direction, and these properties are different than the properties in the radial direction.

Table 5. Thermal conductivity for Evans model (reference: [29] and errata to [29])

	Conductivity component	A_1	A_2	A_3	A_4	A_5	A_6	A_7
Anisotropy	k_{buffer}^{rad}	7.9234×10^{-20}	-4.5698×10^{-16}	1.0671×10^{-12}	-1.3093×10^{-9}	9.3005×10^{-7}	-4.1173×10^{-4}	0.1417
	k_{buffer}^{tan}	8.0582×10^{-19}	-4.6473×10^{-15}	1.085×10^{-11}	-1.3312×10^{-8}	9.4482×10^{-6}	-4.1686×10^{-3}	1.3364
	k_{PyC}^{rad}	6.0638×10^{-19}	-3.4973×10^{-15}	8.1667×10^{-12}	-1.0020×10^{-8}	7.1177×10^{-6}	-3.1510×10^{-3}	1.0841
	k_{PyC}^{tan}	6.1670×10^{-18}	-3.5566×10^{-14}	8.3047×10^{-11}	-1.0188×10^{-7}	7.2308×10^{-5}	-3.1903×10^{-2}	10.227
Isotropy	k_{buffer}	2.6443×10^{-19}	-1.5251×10^{-15}	3.5612×10^{-12}	-4.3691×10^{-9}	3.1024×10^{-6}	-1.3715×10^{-3}	0.4519
	k_{PyC}	2.0237×10^{-18}	-1.1672×10^{-14}	2.7254×10^{-11}	-3.3437×10^{-8}	2.3743×10^{-5}	-1.0496×10^{-2}	3.4585

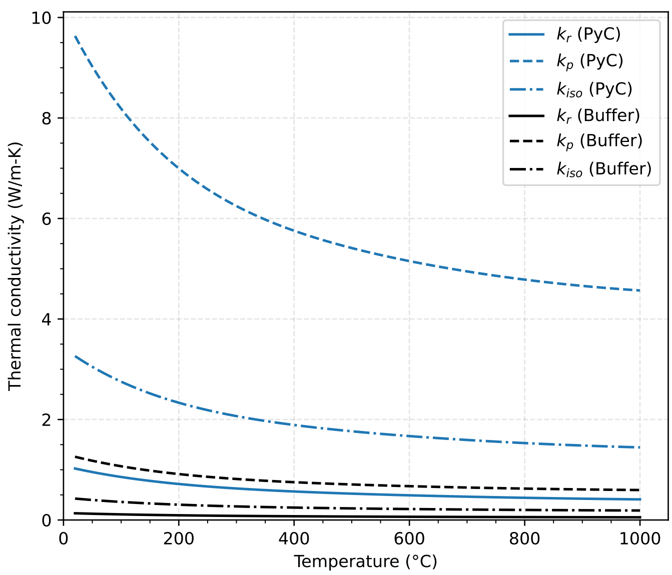

Figure 4. Thermal conductivity of the buffer and PyC coating layers in the TRISO particle as a function of temperature [29].

2.3.3. Weibull Model Parameters of TRISO Coating Layers

The failure probability of the layers is calculated using the Weibull failure probability model represented through Eq. 3. The Weibull characteristic strength and Weibull modulus for the SiC and PyC layers are based on reference [3]. The characteristic strength σ_o for the PyC is a function of the BAF (X) and is expressed as in Eq. 4 with units of MPa-m$^{3/9.5}$.

$$P_f = 1 - exp\left(-\int_V \left(\frac{\sigma}{\sigma_o}\right)^m dV\right) \tag{3}$$

$$\sigma_o = (154.46X^2 - 141.1X)\{(1 + 0.23\phi)[1 + 0.00015(T - 20)]\}^{0.5} \tag{4}$$

where ϕ (10^{25} n/m^2, E >0.18 MeV) is the fast neutron fluence and T (°C) is the temperature. The Weibull modulus for PyC is considered to be a constant 9.5. The characteristic strength and Weibull modulus of the SiC layer are considered to be a constant 9.64 MPa-m$^{3/6}$ and 6, respectively.

2.3.4. Density of TRISO Coating Layers

The initial densities of the buffer, PyC, and SiC layers were considered to be 1050 kg/m^3, 1900 kg/m^3, and 3200 kg/m^3, respectively. The change in densities of the layers over the course of irradiation has been considered in the analysis.

In reality, the texture of the carbon layers, measured through the BAF, changes with irradiation and temperature [39]. In this work, the texture is considered to remain constant throughout the fuel cycle due to lack of a well-defined relationship between the BAF and neutron fluence. The finite element model accounts for the decoupling between the buffer layer and the IPyC layer, which occurs when the buffer layer shrinks during irradiation. However, no decoupling is considered between the SiC and PyC layers.

2.4. Constitutive Equations

The constitutive relationship between the stress and strain components for an anisotropic material is described through Eq. 5.

$$
\begin{bmatrix} \sigma_{rr} \\ \sigma_{\theta\theta} \\ \sigma_{\phi\phi} \\ \sigma_{\theta\phi} \\ \sigma_{\phi r} \\ \sigma_{r\theta} \end{bmatrix}
=
\begin{bmatrix}
\frac{1-\nu_{\theta\phi}\nu_{\phi\theta}}{E_\theta E_\phi \Delta} & \frac{\nu_{\theta r}+\nu_{\phi r}\nu_{\theta\phi}}{E_\theta E_\phi \Delta} & \frac{\nu_{\phi r}+\nu_{\theta r}\nu_{\phi\theta}}{E_\theta E_\phi \Delta} & 0 & 0 & 0 \\
\frac{\nu_{r\theta}+\nu_{r\phi}\nu_{\phi\theta}}{E_\phi E_r \Delta} & \frac{1-\nu_{\phi r}\nu_{r\phi}}{E_\phi E_r \Delta} & \frac{\nu_{\phi\theta}+\nu_{\phi r}\nu_{r\theta}}{E_\phi E_r \Delta} & 0 & 0 & 0 \\
\frac{\nu_{r\phi}+\nu_{r\theta}\nu_{\theta\phi}}{E_r E_\theta \Delta} & \frac{\nu_{\theta\phi}+\nu_{r\phi}\nu_{\theta r}}{E_r E_\theta \Delta} & \frac{1-\nu_{r\theta}\nu_{\theta r}}{E_r E_\theta \Delta} & 0 & 0 & 0 \\
0 & 0 & 0 & G_{\theta\phi} & 0 & 0 \\
0 & 0 & 0 & 0 & G_{\phi r} & 0 \\
0 & 0 & 0 & 0 & 0 & G_{r\theta}
\end{bmatrix}
\begin{bmatrix} \epsilon_{rr} \\ \epsilon_{\theta\theta} \\ \epsilon_{\phi\phi} \\ \gamma_{\theta\phi} \\ \gamma_{\phi r} \\ \gamma_{r\theta} \end{bmatrix}
\tag{5}
$$

where σ is the Cauchy stress, ν is Poisson's ratio, ϵ is the normal strain, γ is the engineering shear strain, G is the shear modulus, E is Young's modulus, r represents the radial component, θ represents the polar angle, ϕ represents the azimuthal angle, and Δ is expressed through Eq. 6 and Eq. 7:

$$
\Delta = \frac{1 - \nu_{r\theta}\nu_{\theta r} - \nu_{\theta\phi}\nu_{\phi\theta} - \nu_{r\phi}\nu_{\phi r} - 2\nu_{r\theta}\nu_{\theta\phi}\nu_{\phi r}}{E_r \, E_\theta \, E_\phi}
\tag{6}
$$

with

$$
\frac{\nu_{\theta r}}{E_\theta} = \frac{\nu_{r\theta}}{E_r} \qquad \frac{\nu_{\phi r}}{E_\phi} = \frac{\nu_{r\phi}}{E_r} \qquad \frac{\nu_{\theta\phi}}{E_\theta} = \frac{\nu_{\phi\theta}}{E_\phi}
\tag{7}
$$

The layers in the TRISO particle are considered to be transversely isotropic with the properties in all directions within a given spherical tangent plane being the same. For representing the tangent plane, we use the subscript p. By replacing the θ and ϕ subscripts with p in the stiffness matrix, we obtain the constitutive relation for the stress and strain for the transverse isotropic material as expressed through Eq. 8.

$$
\begin{bmatrix} \sigma_{rr} \\ \sigma_{\theta\theta} \\ \sigma_{\phi\phi} \\ \sigma_{\theta\phi} \\ \sigma_{\phi r} \\ \sigma_{r\theta} \end{bmatrix}
=
\begin{bmatrix}
\frac{1-\nu_p^2}{E_p^2 \Delta} & \frac{\nu_{pr}+\nu_{pr}\nu_p}{E_p^2 \Delta} & \frac{\nu_{pr}+\nu_{pr}\nu_p}{E_p^2 \Delta} & 0 & 0 & 0 \\
\frac{\nu_{rp}+\nu_{rp}\nu_p}{E_p E_r \Delta} & \frac{1-\nu_{pr}\nu_{rp}}{E_p E_r \Delta} & \frac{\nu_p+\nu_{pr}\nu_{rp}}{E_p E_r \Delta} & 0 & 0 & 0 \\
\frac{\nu_{rp}+\nu_{rp}\nu_p}{E_r E_p \Delta} & \frac{\nu_p+\nu_{rp}\nu_{pr}}{E_r E_p \Delta} & \frac{1-\nu_{rp}\nu_{pr}}{E_r E_p \Delta} & 0 & 0 & 0 \\
0 & 0 & 0 & G_p & 0 & 0 \\
0 & 0 & 0 & 0 & G_{pr} & 0 \\
0 & 0 & 0 & 0 & 0 & G_{pr}
\end{bmatrix}
\begin{bmatrix} \epsilon_{rr} \\ \epsilon_{\theta\theta} \\ \epsilon_{\phi\phi} \\ \gamma_{\theta\phi} \\ \gamma_{\phi r} \\ \gamma_{r\theta} \end{bmatrix}
=
\begin{bmatrix}
C_{11} & C_{12} & C_{12} & 0 & 0 & 0 \\
C_{12} & C_{22} & C_{23} & 0 & 0 & 0 \\
C_{12} & C_{23} & C_{22} & 0 & 0 & 0 \\
0 & 0 & 0 & \frac{C_{22}-C_{23}}{2} & 0 & 0 \\
0 & 0 & 0 & 0 & C_{55} & 0 \\
0 & 0 & 0 & 0 & 0 & C_{55}
\end{bmatrix}
\begin{bmatrix} \epsilon_{rr} \\ \epsilon_{\theta\theta} \\ \epsilon_{\phi\phi} \\ \gamma_{\theta\phi} \\ \gamma_{\phi r} \\ \gamma_{r\theta} \end{bmatrix}
\tag{8}
$$

where Δ is expressed through Eq. 9:

$$\Delta = \frac{1 - \nu_{rp}\nu_{pr} - \nu_p^2 - \nu_{rp}\nu_{pr} - \nu_{rp}\nu_p\nu_{pr}}{E_r\, E_p^2} \tag{9}$$

For an isotropic material, the constitutive relation is expressed through Eq. 10.

$$\begin{bmatrix} \sigma_{rr} \\ \sigma_{\theta\theta} \\ \sigma_{\phi\phi} \\ \sigma_{\theta\phi} \\ \sigma_{\phi r} \\ \sigma_{r\theta} \end{bmatrix} = \begin{bmatrix} \frac{E(1-\nu)}{(1+\nu)(1-2\nu)} & \frac{E(\nu)}{(1+\nu)(1-2\nu)} & \frac{E(\nu)}{(1+\nu)(1-2\nu)} & 0 & 0 & 0 \\ \frac{E(\nu)}{(1+\nu)(1-2\nu)} & \frac{E(1-\nu)}{(1+\nu)(1-2\nu)} & \frac{E(\nu)}{(1+\nu)(1-2\nu)} & 0 & 0 & 0 \\ \frac{E(\nu)}{(1+\nu)(1-2\nu)} & \frac{E(\nu)}{(1+\nu)(1-2\nu)} & \frac{E(1-\nu)}{(1+\nu)(1-2\nu)} & 0 & 0 & 0 \\ 0 & 0 & 0 & \frac{E}{2(1+\nu)} & 0 & 0 \\ 0 & 0 & 0 & 0 & \frac{E}{2(1+\nu)} & 0 \\ 0 & 0 & 0 & 0 & 0 & \frac{E}{2(1+\nu)} \end{bmatrix} \begin{bmatrix} \epsilon_{rr} \\ \epsilon_{\theta\theta} \\ \epsilon_{\phi\phi} \\ \gamma_{\theta\phi} \\ \gamma_{\phi r} \\ \gamma_{r\theta} \end{bmatrix} = \begin{bmatrix} C_{11} & C_{12} & C_{12} & 0 & 0 & 0 \\ C_{12} & C_{11} & C_{12} & 0 & 0 & 0 \\ C_{12} & C_{12} & C_{11} & 0 & 0 & 0 \\ 0 & 0 & 0 & \frac{C_{11}-C_{12}}{2} & 0 & 0 \\ 0 & 0 & 0 & 0 & \frac{C_{11}-C_{12}}{2} & 0 \\ 0 & 0 & 0 & 0 & 0 & \frac{C_{11}-C_{12}}{2} \end{bmatrix} \begin{bmatrix} \epsilon_{rr} \\ \epsilon_{\theta\theta} \\ \epsilon_{\phi\phi} \\ \gamma_{\theta\phi} \\ \gamma_{\phi r} \\ \gamma_{r\theta} \end{bmatrix} \tag{10}$$

For anisotropic thermal conductivity, the relationship between the heat flux components (q_r, q_θ, q_ϕ) and the temperature gradient components (dT/dr, $dT/(r\,d\theta)$, $dT/(r\,sin\theta\,d\phi)$) are described through Eq. 11, where k_{rr} and k_p are the radial and tangential plane components of thermal conductivity.

$$\begin{bmatrix} q_r \\ q_\theta \\ q_\phi \end{bmatrix} = \begin{bmatrix} -k_{rr} & 0 & 0 \\ 0 & -k_p & 0 \\ 0 & 0 & -k_p \end{bmatrix} \begin{bmatrix} \frac{dT}{dr} \\ \frac{dT}{r\,d\theta} \\ \frac{dT}{r\,sin\theta\,d\phi} \end{bmatrix} \tag{11}$$

2.5. Simulations

As discussed earlier, the thermal and elastic properties of the TRISO layers should exhibit anisotropy if the microstructures are textured. The impact of anisotropy on the stresses and failure probability is analyzed using simulations performed in the fuel performance code BISON. In these simulations, two cases are considered: (1) all the TRISO layers are considered to be isotropic and (2) all the TRISO layers are considered to be anisotropic. These simulations were performed for spherical TRISO particles, as shown in Figure 1. These simulations do not consider crack in the IPyC layer, so the reported failure probability of the SiC layer is based on the assumption that IPyC layer remains intact.

3. Results

In this section, the results for spherical TRISO particles are presented. A discussion on the comparison between the spherical and aspherical particles is presented in Section 4.5. Figure 5 shows a schematic of the radial and tangential stresses at a point in a TRISO coating layer. Figures 6 – 13 show the results of the analyses. Figure 6 shows the radial and tangential stress distribution in the PyC and SiC layers of the TRISO particle with anisotropic properties. Figures 7, 9, and 11 show the distribution of stresses in the IPyC, OPyC, and SiC layers, respectively. The stress distribution for the case with isotropic properties (not shown here) is similar to the case with anisotropic properties, although stress magnitudes are different.

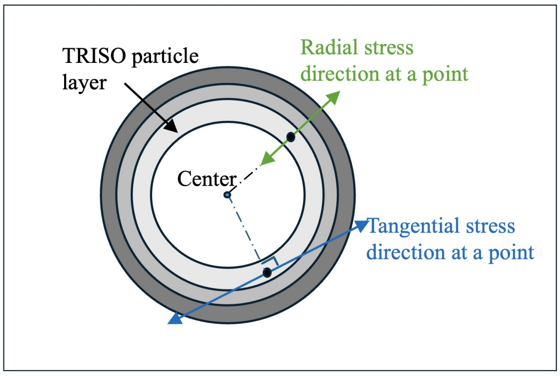

Figure 5. The radial and tangential directions at a point in a TRISO coating layer. The ”radial stress” is the stress component along the radial direction and ”tangential stress” is the stress component along the tangential direction at a point in the coating layer.

Figures 8, 10, and 12 show the variation of stresses with neutron fluence in the IPyC, OPyC, and SiC layers, respectively, at the locations where stress magnitudes were found to be greatest during the entire operating time. Figure 13 shows the variation of failure probability of the IPyC and SiC layers with fluence. It is clear from these results that the stresses reach their peak magnitudes earlier for the anisotropic case. The peak magnitudes for radial stresses do not differ much between the two cases, but the peak magnitudes for tangential stresses differ by about 5-15 MPa.

For the IPyC layer, the maximum difference in the radial stress occurs initially (neutron fluence $<5.86\times10^{24}$ n/m^2) when the stress is increasing or towards the end of operation when the neutron fluence is 5.6×10^{25} n/m^2. The difference in the maximum tangential stresses during the operation is more significant (up to about 25 MPa) than that in the maximum radial stresses (about 7 MPa).

The difference in the radial stresses for the isotropic and anisotropic cases in the OPyC layer is negligible. However, for tangential stresses, a difference in the stress magnitudes of up to 15 MPa is seen. Similar to the IPyC layer, the neutron fluence at which the stresses reach their peak value is slightly different: 8.0×10^{24} n/m^2 for the isotropic case and 5.9×10^{24} n/m^2 for the anisotropic case.

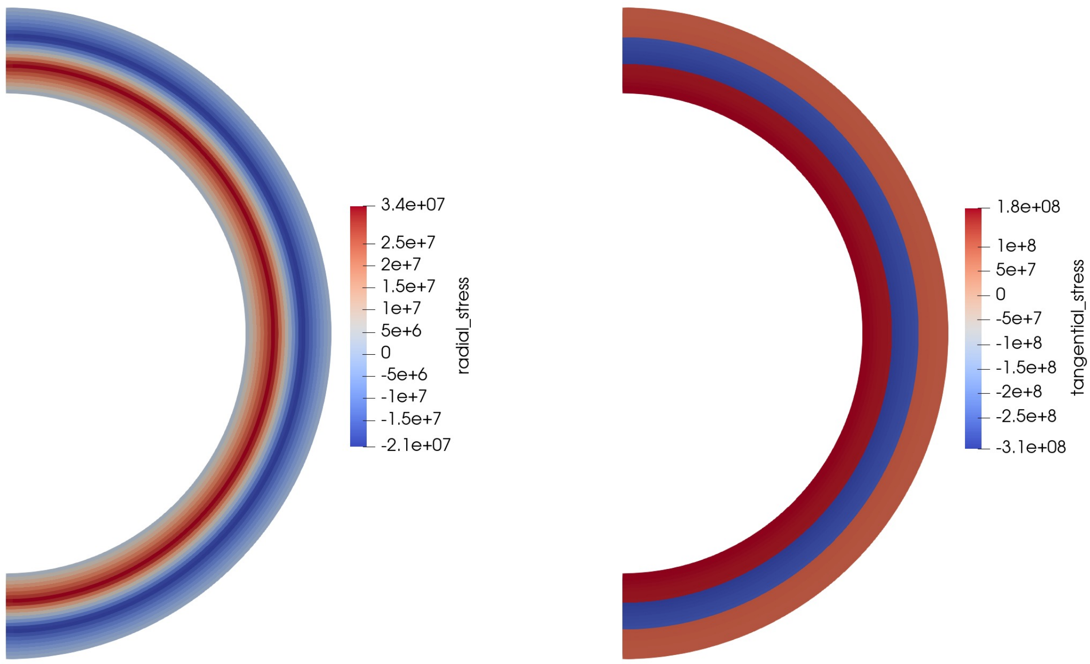

Figure 6. Distribution of radial and tangential stresses (units: Pa) in the TRISO particle PyC and SiC with all layers considered anisotropic at time $5.1{\times}10^6$ seconds (fluence = $5.86{\times}10^{24}$ n/m^2).

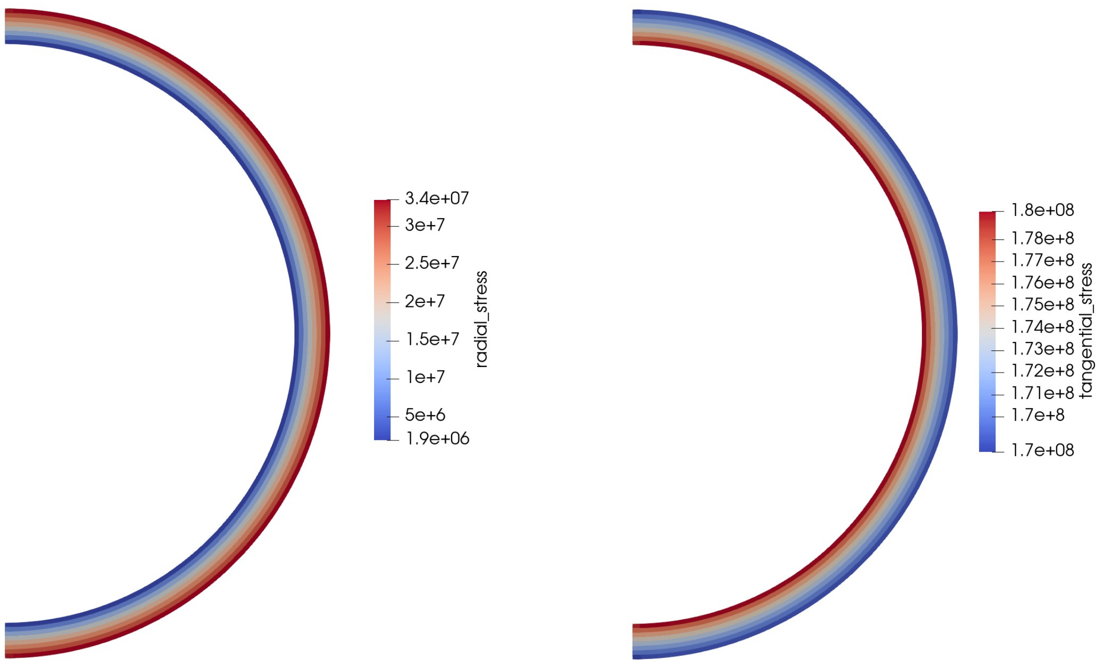

Figure 7. Distribution of radial and tangential stresses (units: Pa) in the IPyC layer with all layers considered anisotropic at time $5.1{\times}10^6$ seconds (fluence = $5.86{\times}10^{24}$ n/m^2).

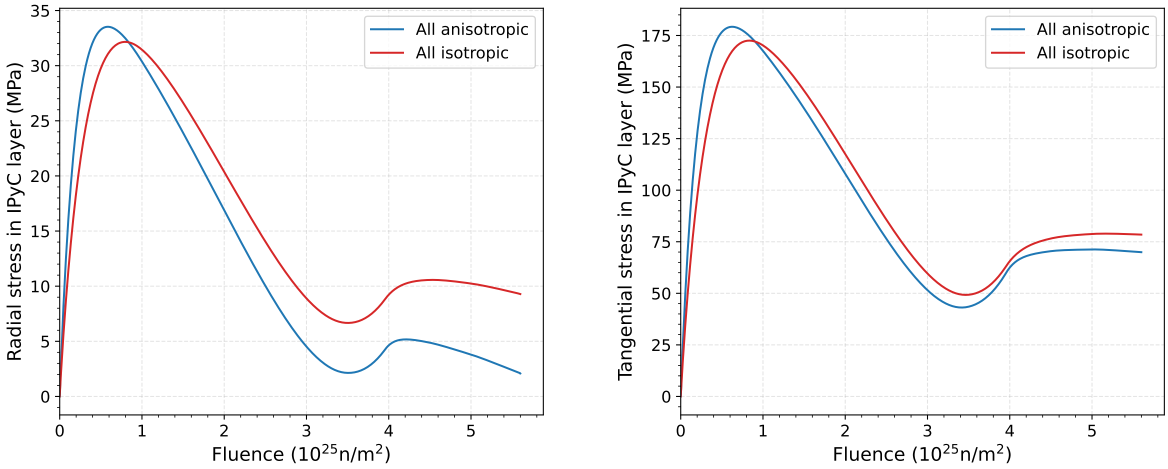

Figure 8. Variation of radial and tangential stresses with fluence in the IPyC layer of the TRISO particle.

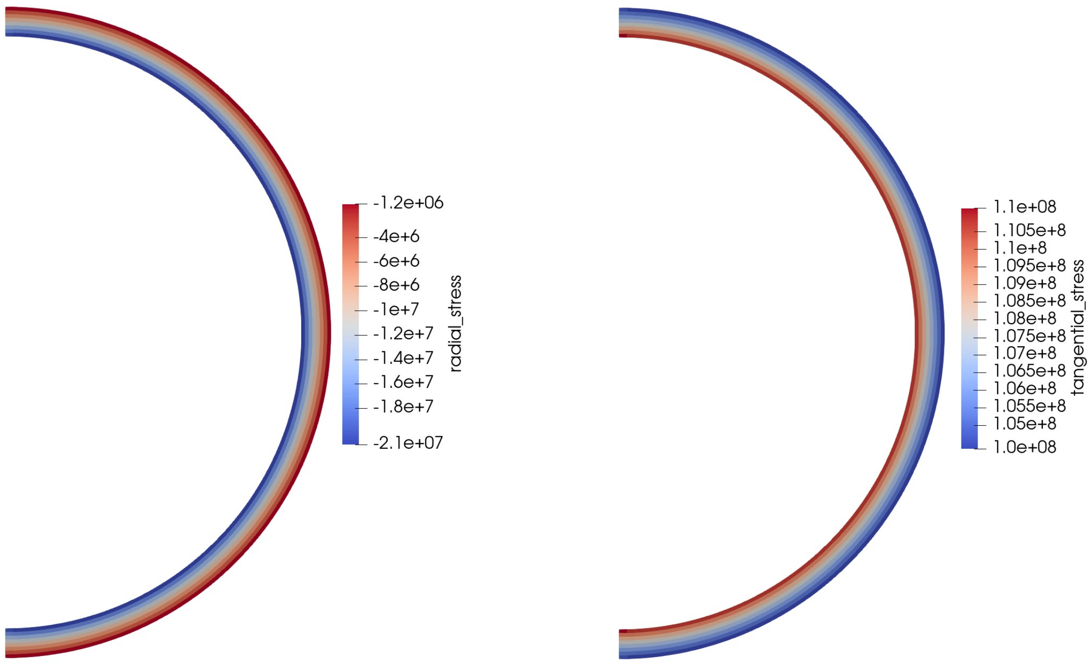

Figure 9. Distribution of radial and tangential stresses (units: Pa) in the OPyC layer with all layers considered anisotropic at time 5.1×10^{6} seconds (fluence = 5.86×10^{24} n/m^2).

Similar to the PyC layers, the difference in the radial stress in the SiC layer for the two cases is small with the difference in the maximum magnitudes being about 2 MPa and the overall maximum difference of about 7 MPa at the end of operation. However, the difference in the tangential stress is significant with the maximum difference of about 50 MPa during the initial operation (neutron fluence $<5.86\times10^{24}$ n/m^2). The Weibull failure probability value of the IPyC layer reaches a maxima of 0.074 after a neutron fluence of 7.7×10^{24} n/m^2 for the isotropic case, which is significantly lower than the maximum failure probability value for the anisotropic case (0.13) that was reached after

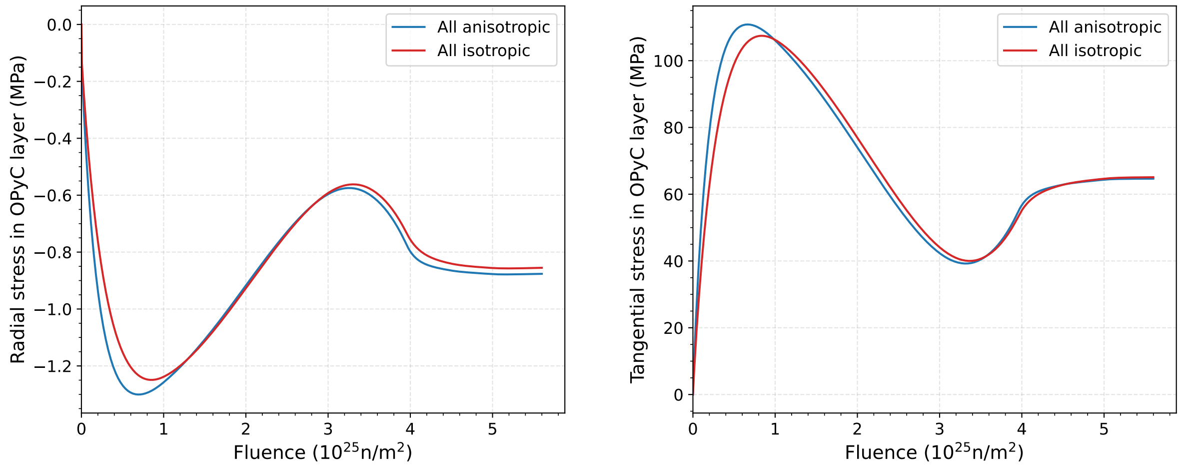

Figure 10. Variation of radial and tangential stresses with fluence in the OPyC layer of the TRISO particle.

a fluence of $5.7{\times}10^{24}$ n/m^2. The difference in the failure probabilities for the two cases is also significant for the SiC layer: $7.1{\times}10^{-9}$ for the isotropic case and $9.2{\times}10^{-9}$ for the anisotropic case.

In general, these results indicate that when anisotropy is not accounted for in the TRISO layers, the tangential stress magnitudes are significantly lower. Consequently, the failure probabilities are significantly lower. A detailed discussion of the contribution of the anisotropies in individual layers and comparisons on the aspherical versus spherical TRISO particle geometry are presented in Section 4.

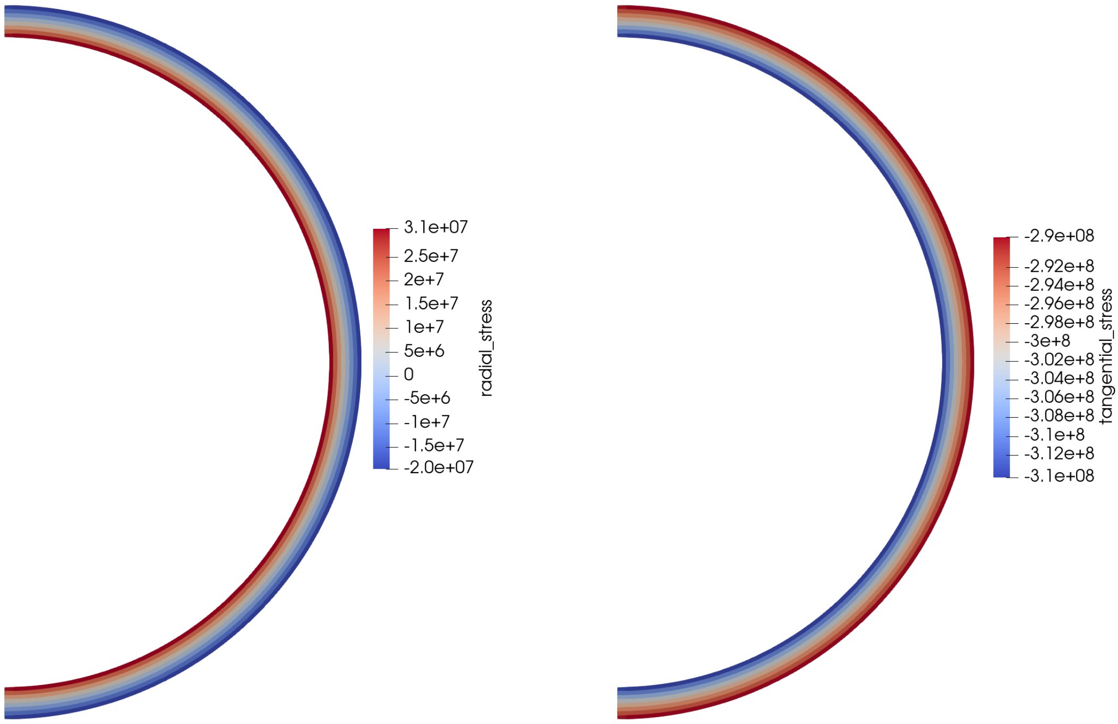

Figure 11. Distribution of radial and tangential stresses (units: Pa) in the SiC layer with all layers considered anisotropic at time 5.1×10^6 seconds (fluence = 5.86×10^{24} n/m^2).

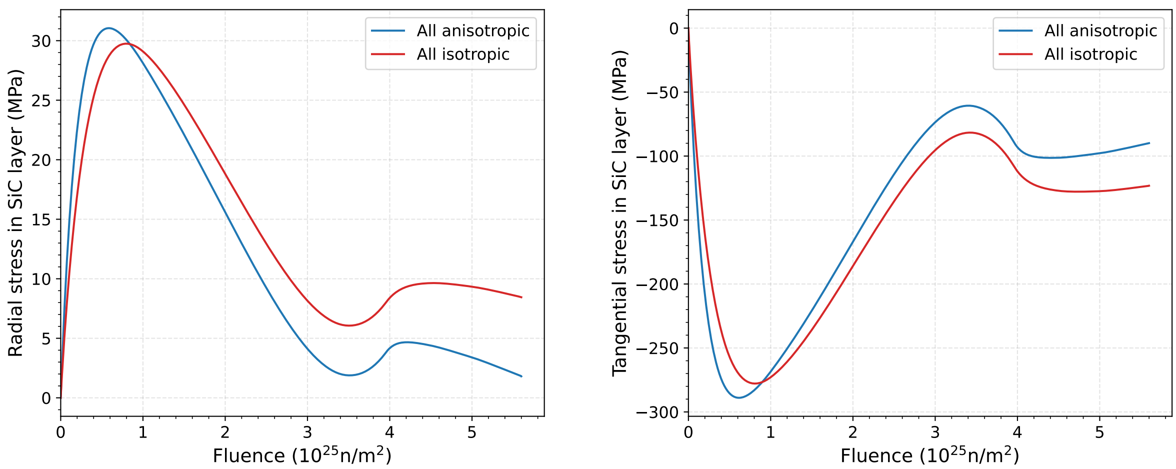

Figure 12. Variation of radial and tangential stresses with fluence in the SiC layer of the TRISO particle.

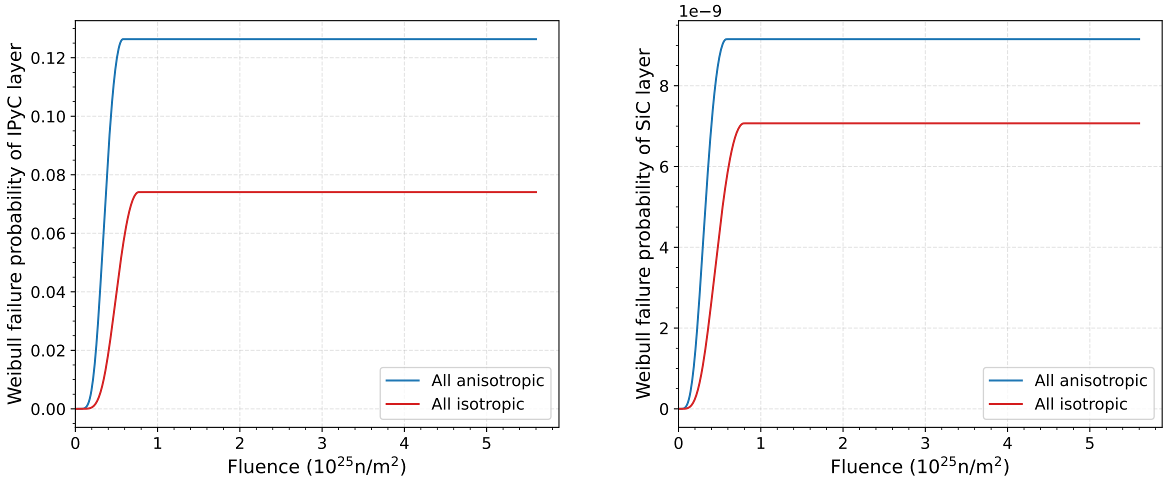

Figure 13. Variation of failure probability of the IPyC and SiC layers with fluence.

4. Discussion

As shown in Section 3, anisotropy has a significant effect on the stresses in the TRISO layers and the failure probability of the PyC and SiC layers. In this section, the individual effects of the anisotropy in the thermal and elastic properties of the TRISO layers are presented and discussed. These effects are analyzed through several simulations performed with particular sets of TRISO material properties as listed below.

1. Thermal anisotropy considered in the PyC layers and all other properties are considered to be isotropic.
2. Elasticity anisotropy considered in the PyC layers and all other properties are considered to be isotropic.
3. Thermal anisotropy considered in the buffer layer and all other properties are considered to be isotropic.
4. Elasticity anisotropy considered in the buffer layer and all other properties are considered to be isotropic.
5. Elasticity anisotropy considered in the SiC layer and all other properties are considered to be isotropic.

These simulations assume spherical geometry for the TRISO particle. Section 4.5 includes the aspherical particle as well because it focuses on understanding the impact of asphericity on the stresses and failure probability.

4.1. Effect of Anisotropic Thermal Properties of PyC

Figure 14 shows the effect of considering anisotropy in the thermal properties of PyC layers on the tangential stresses and temperature in the IPyC layer. For the anisotropic case, the radial thermal conductivity is lower compared with the isotropic case (see Figure 4 in Section 2.3.2) which results in an increase in its temperature at the inner surface of the IPyC layer by about 11 K (from 1278 K to 1289 K) and an increase in temperature difference across the IPyC thickness by roughly 6 K (from 4 K to 10 K). The temperature at the center of kernel is 1442 K for the all-isotropic case and 1453 K for the case with anisotropic thermal properties of PyC at the end of operation (neutron fluence = 5.6×10^{25} n/m^2).

Higher temperature leads to greater creep, resulting in a slight decrease in the layer stresses. The maximum tangential stress in the IPyC layer for the anisotropic case is lower by about 4 MPa compared to the isotropic case. Figure 15 shows the effect on the Weibull failure probability of IPyC and SiC layers. The Weibull failure probability of the IPyC layer decreases by 0.01 ($\approx$14%), while the SiC layer decreases by 5×10^{-10} ($\approx$ 7%). Since the SiC layer is attached to the PyC layers and stresses in the SiC layer are driven by the deformation of PyC layers, the reduced deformation and stresses in the PyC layers lead to reduced stresses in the SiC layer as well. Note that these results do not consider delamination between the PyC and SiC layers.

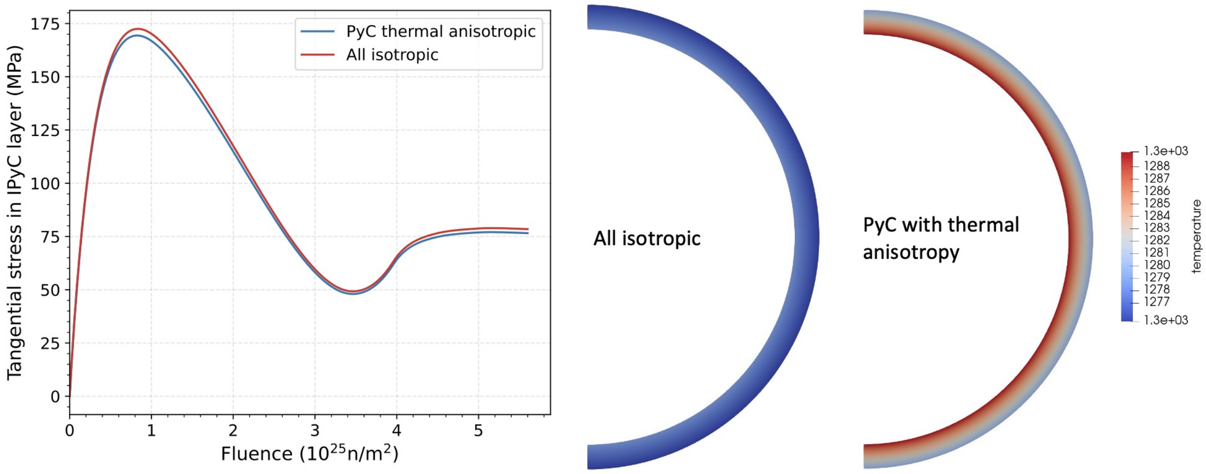

Figure 14. Comparison of tangential stresses and temperature in the IPyC layer for the cases with all layers isotropic and PyC layers having anisotropic thermal properties.

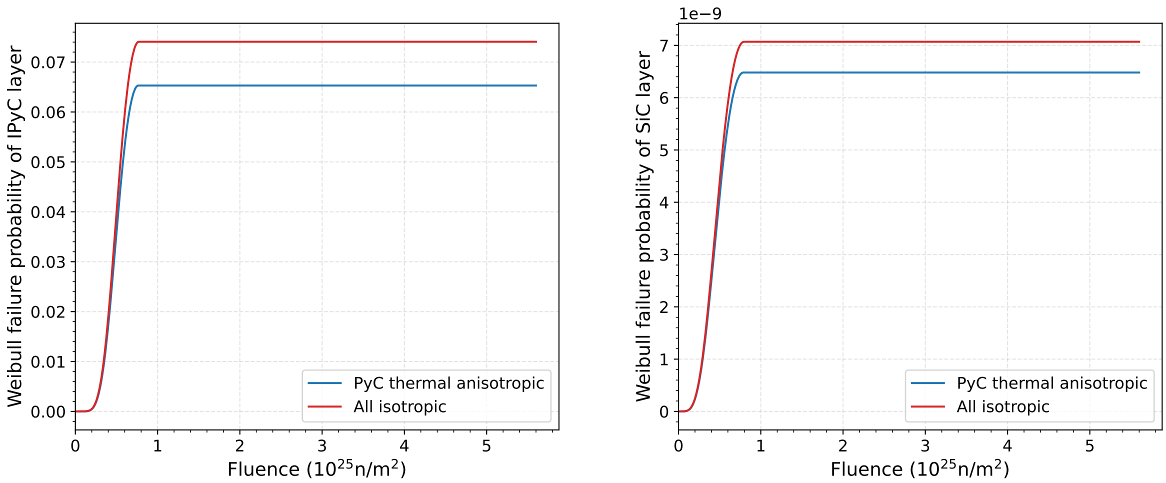

Figure 15. Comparison of the Weibull failure probability of (a) the IPyC layer and (b) the SiC layer for the case with the isotropic properties assumed in all the TRISO layers and the case with the anisotropic thermal properties considered only in the PyC layers and all other properties assumed to be isotropic.

4.2. *Effect of Anisotropic Elastic Properties of PyC*

Figures 16, 17, and 18 show the effect of anisotropic elastic properties on the radial and tangential stresses in the IPyC, OPyC, and SiC layers, respectively. The stresses are higher in magnitude for the case with anisotropic elasticity in general with the greatest difference occurring initially (neutron fluence $<5.86\times10^{24}$ n/m^2). The higher stresses for the anisotropic case leads to an increase of 93% (0.075 to 0.14) in the failure probability of the IPyC and increase of 50% (7×10^{-9} to 1.05×10^{-8}) in the failure probability of SiC layers compared to the all-isotropic case, as shown in Figure 19. It can be noted that the impact of anisotropic elastic properties of the PyC layers on the stresses is much greater than the impact of the anisotropic thermal properties.

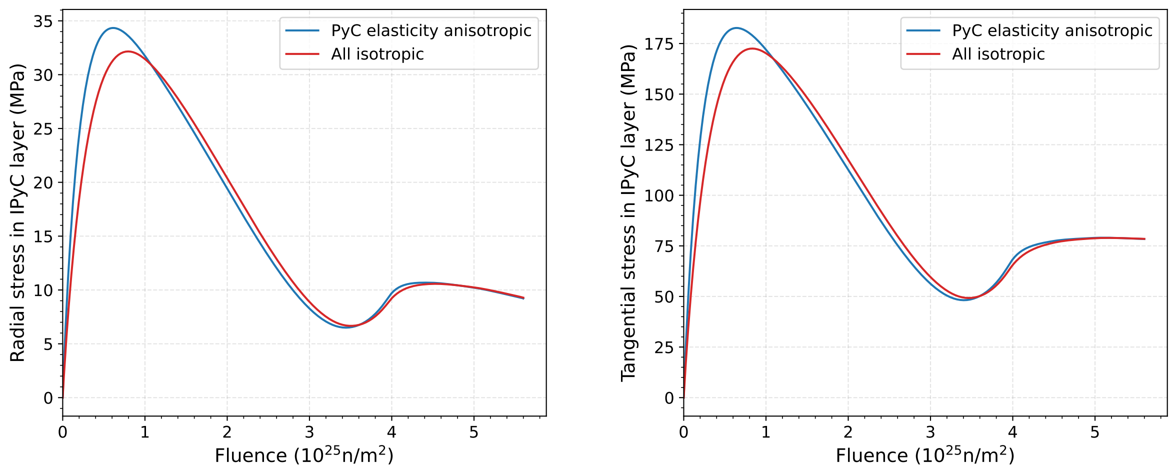

Figure 16. Comparison of the radial and tangential stresses in the IPyC layer for the case with isotropic properties assumed in all the TRISO layers and the case with anisotropic elastic properties considered only in the PyC layers.

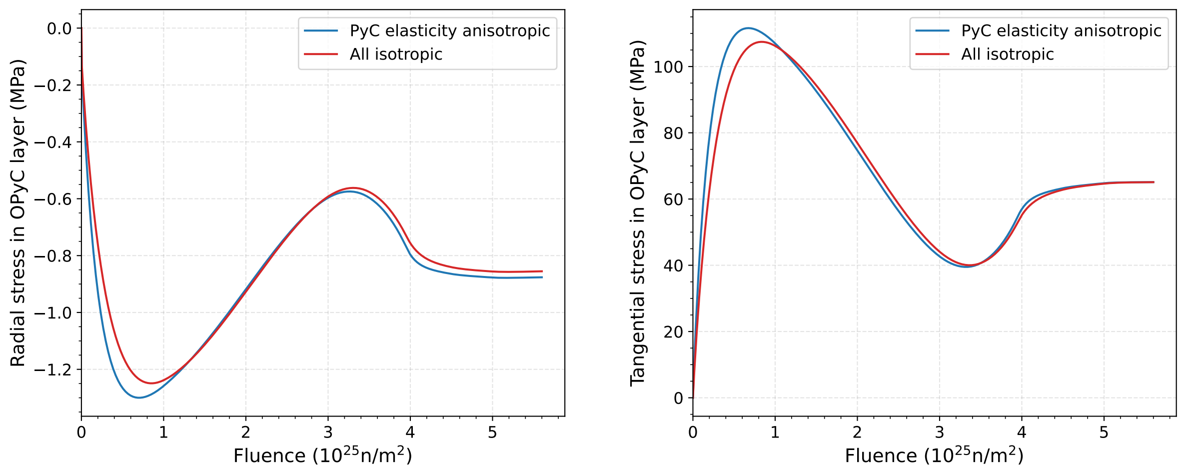

Figure 17. Comparison of the radial and tangential stresses in the OPyC layer for the case with isotropic properties assumed in all the TRISO layers and the case with anisotropic elastic properties considered only in the PyC layers.

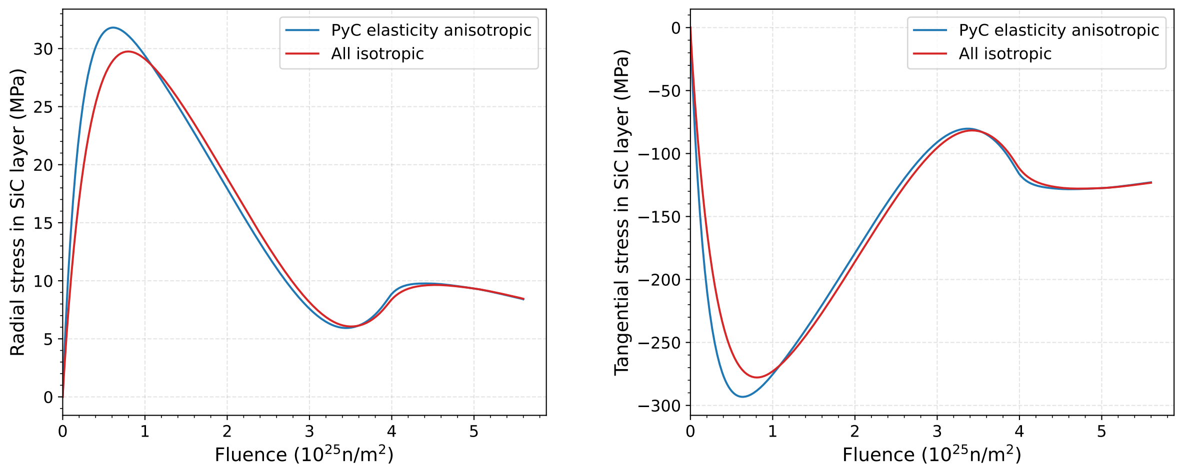

Figure 18. Comparison of the radial and tangential stresses in the SiC layer for the case with isotropic properties assumed in all the TRISO layers and the case with anisotropic elastic properties considered only in the PyC layers.

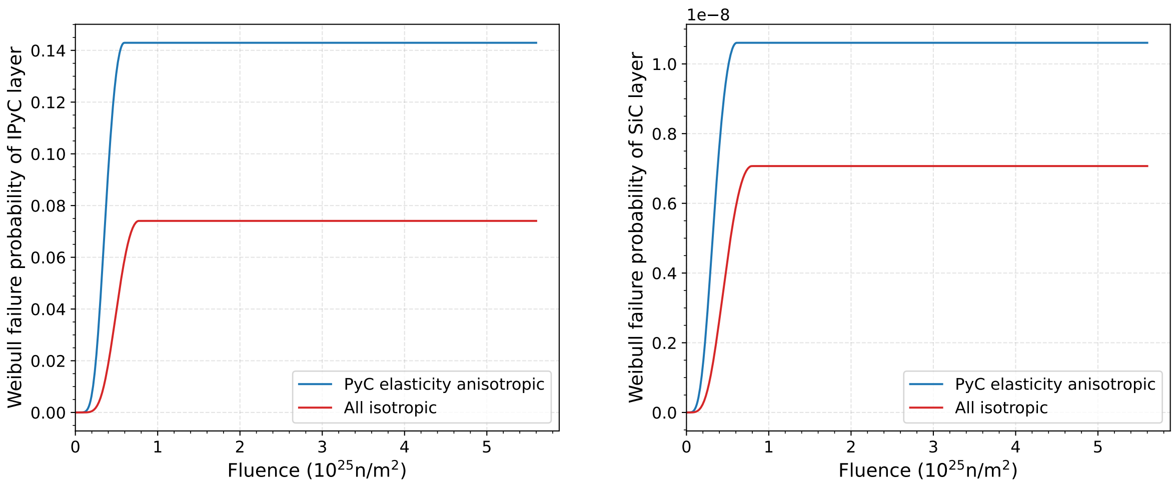

Figure 19. Comparison of the Weibull failure probability of (a) the IPyC layer and (b) the SiC layer for the case with the isotropic properties assumed in all the TRISO layers and the case with the anisotropic elastic properties considered only in the PyC layers.

4.3. *Effect of Anisotropic Thermal and Elastic Properties of Buffer*

Figure 20 shows the temperature distribution in the fuel particles for the case with all the TRISO isotropic layers and the case with only the buffer layer having the anisotropic thermal properties. For the anisotropic case, the radial thermal conductivity of buffer is lower compared with the isotropic case (see Figure 4 in Section 2.3.2) which results in an increase in the temperature gradient across buffer as well as higher fuel temperature. It can be noted from the figure that the temperature of the kernel for the case with the thermally anisotropic buffer is about 200 K higher than for the case with all the isotropic layers. Due to the higher temperature, the fission gas release and resultant gas pressure on the IPyC layer is greater. The increased gas pressure also changes the stresses and failure probability, as shown in Figures 21, 22, and 23. The difference in the stresses increase with operation time due to greater fission gas release rate for the anisotropic case. The effect of anisotropic elastic properties of the buffer on the stresses in the PyC and SiC layers was found to be negligible; those results are not shown here.

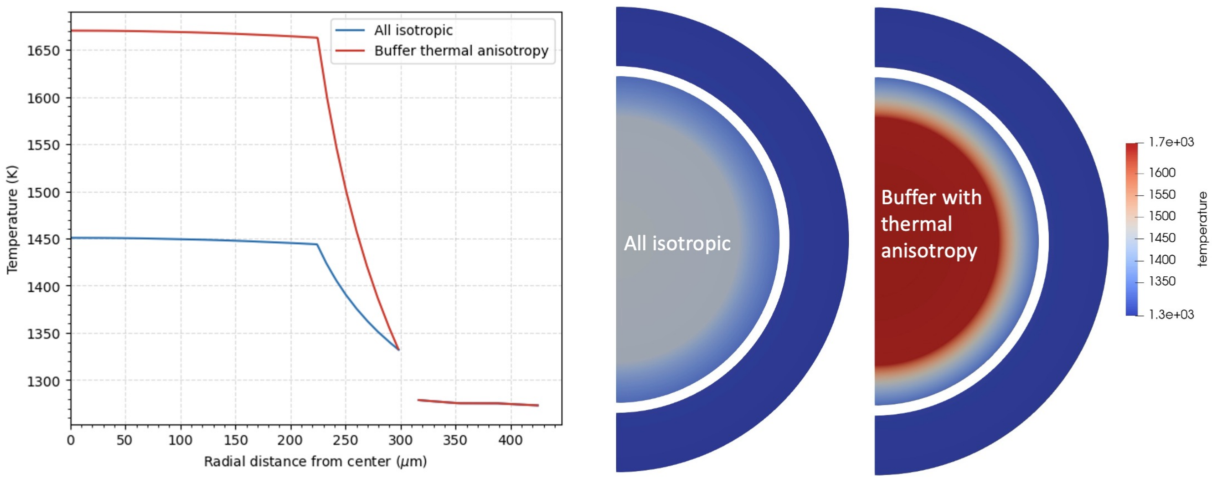

Figure 20. Comparison of the cases with all the isotropic layers and the buffer layer having anisotropic thermal properties. Temperature distribution shown for 7.2 months of operation. Note that the white space between the buffer and the IPyC layer is the gap between the two layers which develops due to shrinkage of the buffer layer under irradiation over time

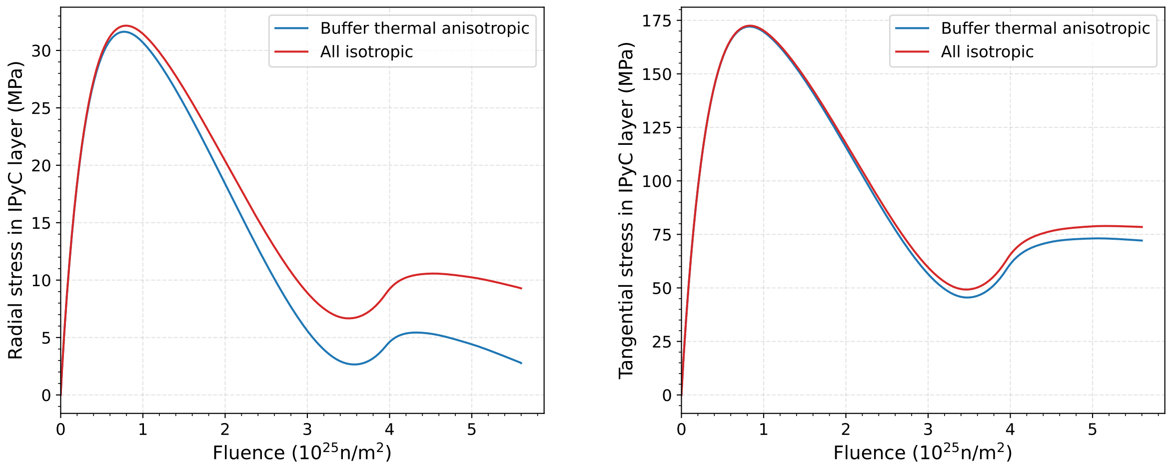

Figure 21. Comparison of the radial and tangential stresses in the IPyC layer for the case with the isotropic properties assumed in all the TRISO layers and the case with the anisotropic thermal properties considered only in the buffer layer.

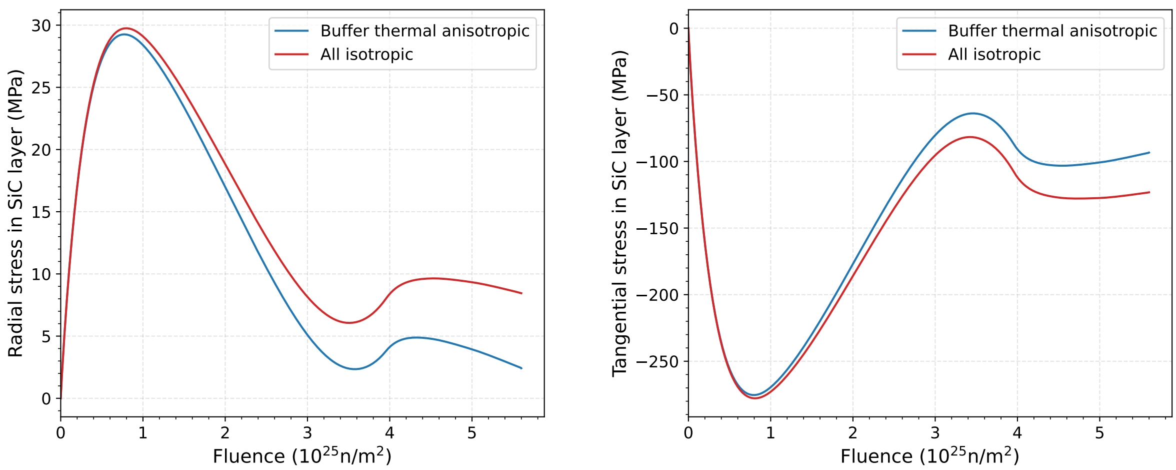

Figure 22. Comparison of the radial and tangential stresses in the SiC layer for the case with the isotropic properties assumed in all the TRISO layers and the case with the anisotropic thermal properties considered only in the buffer layer.

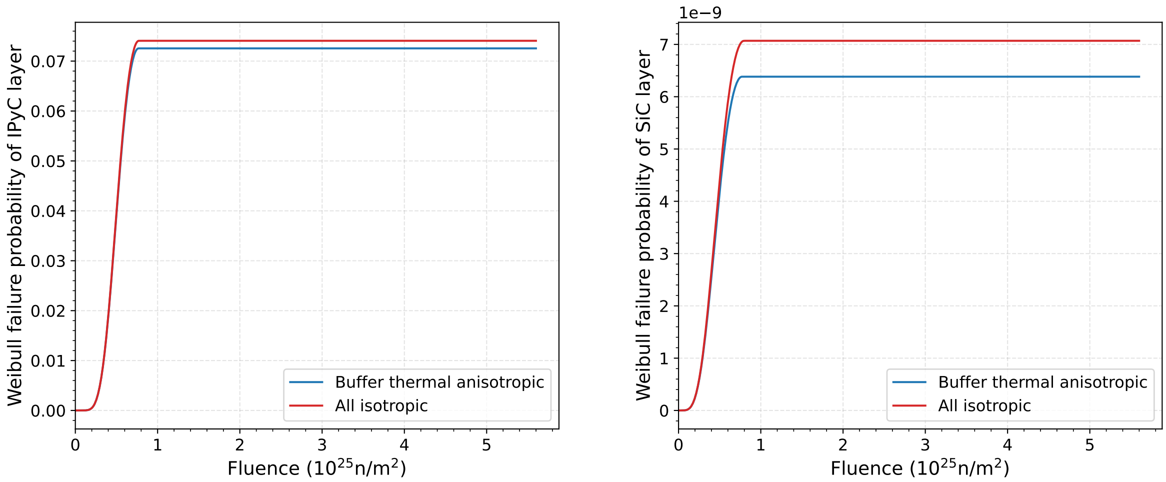

Figure 23. Comparison of the Weibull failure probability of (a) the IPyC layer and (b) the SiC layer for the case with the isotropic properties assumed in all the TRISO layers and the case with the anisotropic thermal properties considered only in the buffer layer.

4.4. *Effect of Anisotropic Elastic Properties of SiC*

The stresses and failure probability in the PyC and SiC layers for the case with the anisotropic elastic properties for SiC were found to be very similar to those of the case with the isotropic elastic properties providing only a slight increase in the failure probability for the anisotropic case, as shown in Figure 24.

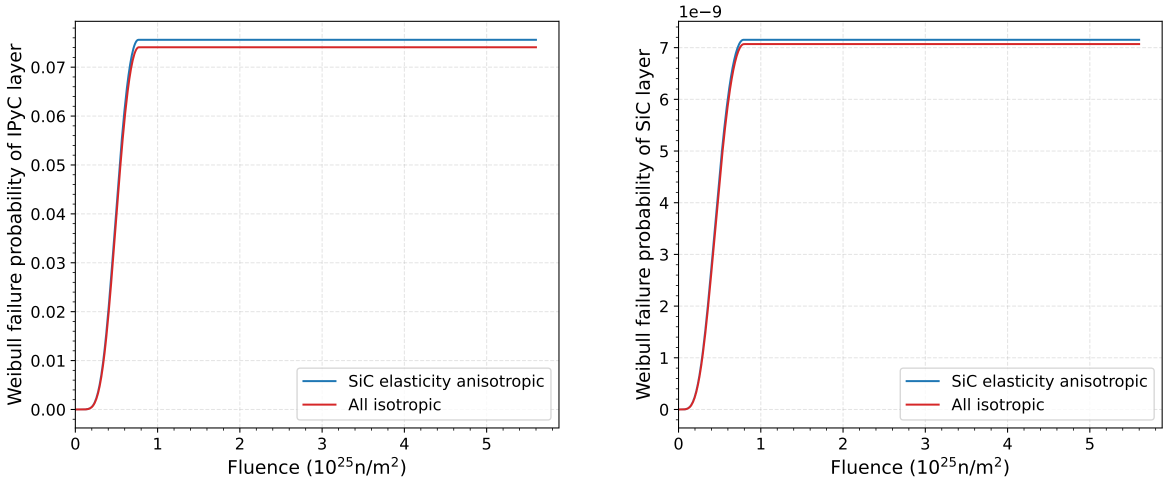

Figure 24. Comparison of the Weibull failure probability of (a) the IPyC layer and (b) the SiC layer for the case with the isotropic properties assumed in all the TRISO layers and the case with the anisotropic elastic properties considered only in the SiC layer.

4.5. *Spherical vs. Aspherical Particle*

In this section, we present the comparison of TRISO fuel performance for the isotropic and anisotropic properties in context of geometry of the particle: spherical and aspherical geometries. The asphericity of the particle is measured as aspect ratio. The aspect ratio, A, is defined as:

$$A = \frac{2R}{R + \sqrt{R^2 - r^2}} \tag{12}$$

where R is the largest radius of the particle and r is the distance of the particle center from the center of outer surface of the flat region. We assumed an aspect ratio of 1.04 for this study. As for the other simulations, the decoupling between the buffer and the IPyC layer was considered in these simulations as well.

Figures 25 – 29 show the comparison of the stresses and failure probabilities for spherical and aspherical TRISO particles. These figures indicate that the stresses in the spherical particle are much smaller as compared with the aspherical particle. The reduced stresses for the spherical particle can be attributed to the lack of stress concentration, which is present in the aspherical particle. Not only are the tensile stresses lower for the spherical particle, the compressive stresses (tangential stress in the SiC layer) are greater in magnitude leading to greater resistance for particle failure. For the same reasons, the failure probabilities for the PyC and SiC layers are also much greater for the aspherical particle for both isotropic and anisotropic cases: for PyC layer the failure probability increases from 12.5% to 16% for anisotropic case and 7.4% to 21.3% for isotropic case; and for SiC layer the failure probability increases from 9.1×10^{-7}% to 6.8×10^{-6}% for anisotropic case and 7.1×10^{-7}% to 2.2×10^{-5}% for isotropic case. Note that these results depends on the geometry chosen for the aspherical particle. More realistic geometries for aspherical particle with smoother transitions in the layers' radii would likely exhibit better structural integrity than the particles with sharper transitions in the layers' radii. An interesting finding from this study is that the effect of the anisotropic properties on the maximum stresses and failure probability depends on the geometry. As discussed in Section 3, the stresses and failure probability of the TRISO layers are higher for the anisotropic case for the spherical geometry, while for the aspherical geometry, the stresses and failure probability are lower for the anisotropic case. It seems that not only the contribution of geometry to the stresses in the TRISO layers (and consequently to the failure probability of the particle) is significant, but the geometry also determines whether the anisotropy in the material properties will have a favorable or unfavorable effect on fuel performance.

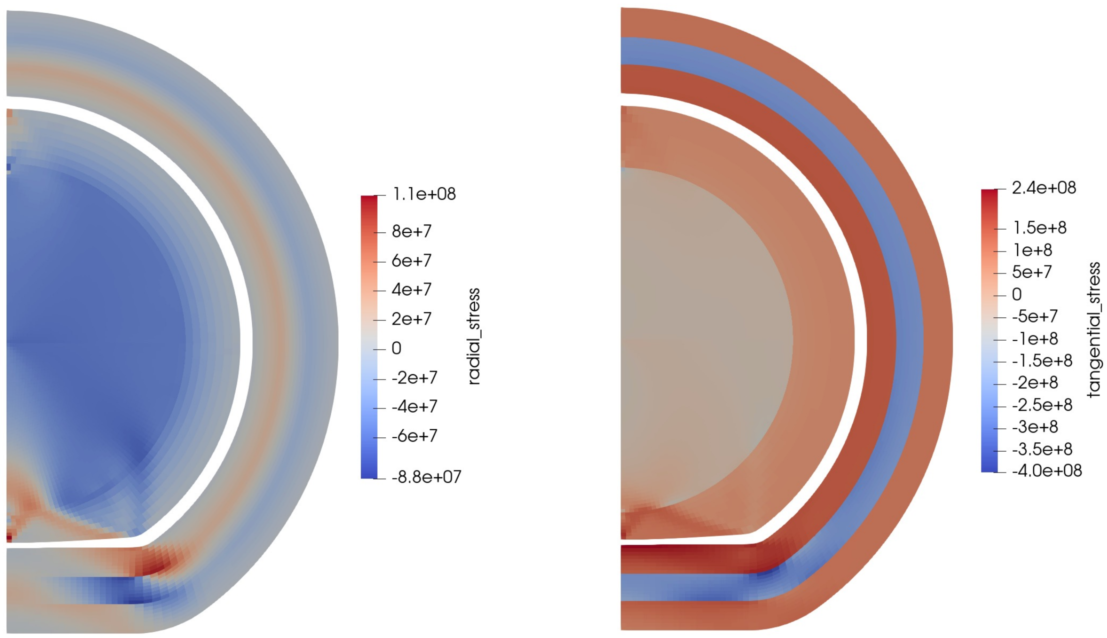

Figure 25. Distribution of radial and tangential stresses (units: Pa) in the TRISO particle with all layers considered anisotropic at time 1.2×10^{7} seconds (fluence = 1.38×10^{25} n/m^2).

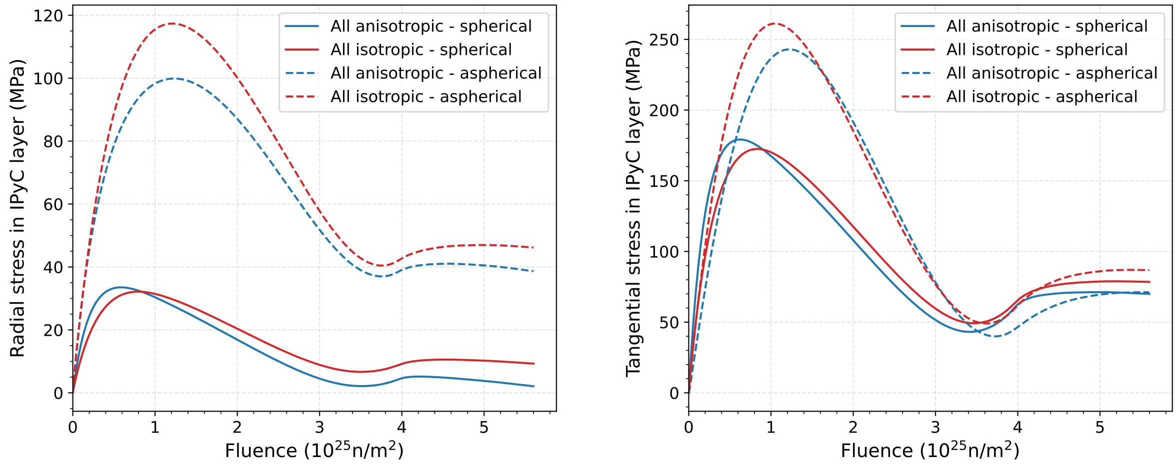

Figure 26. Variation of radial and tangential stresses with fluence in the IPyC layer of the TRISO particle.

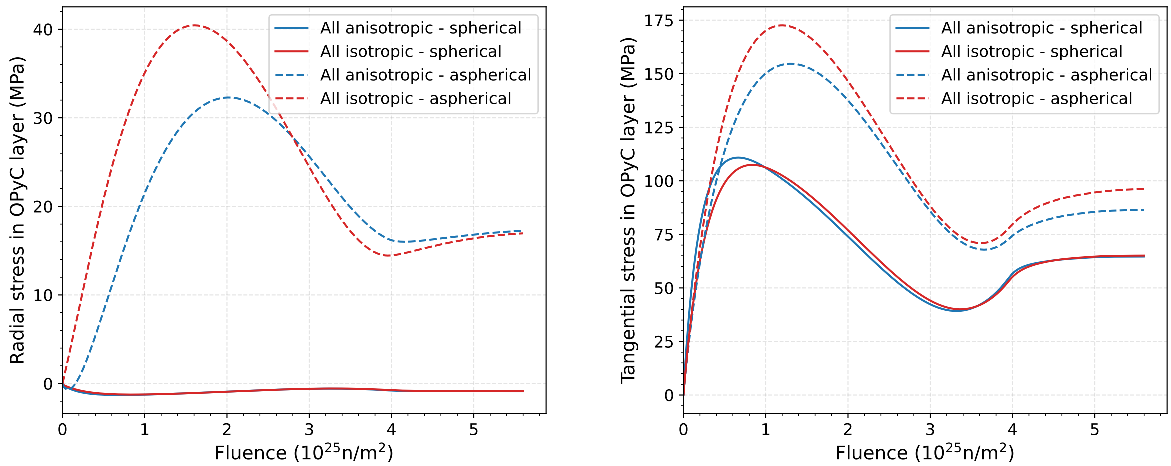

Figure 27. Variation of radial and tangential stresses with fluence in the OPyC layer of the TRISO particle.

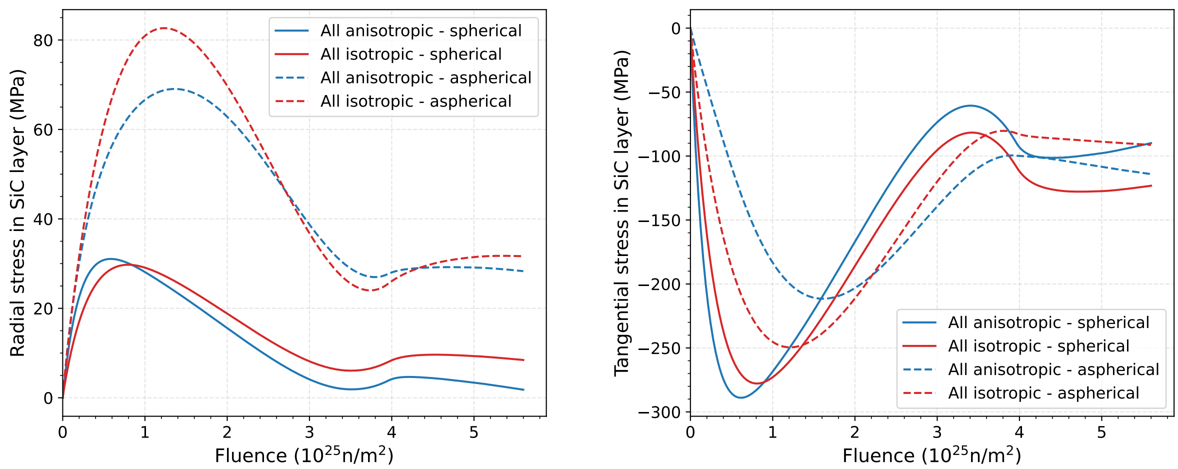

Figure 28. Variation of radial and tangential stresses with fluence in the SiC layer of the TRISO particle.

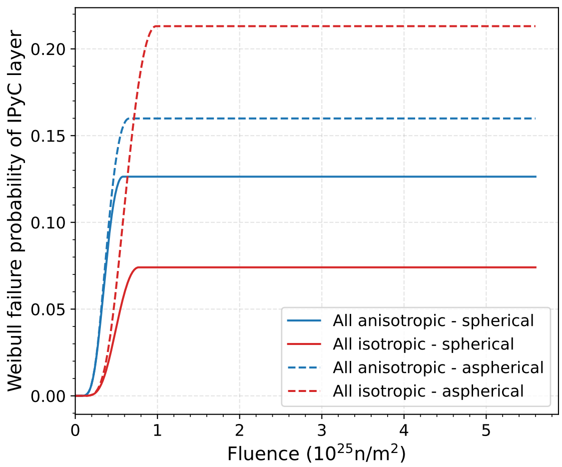

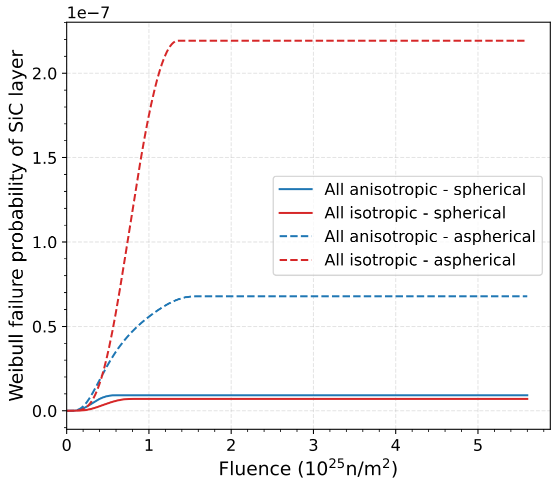

Figure 29. Variation of failure probability of the IPyC and SiC layers with fluence.

4.6. Effect of Temperature

Simulations were performed for different thermal operating conditions to understand the effect of temperature on the particle performance and how temperature influences the anisotropy effects. Three different temperatures—1073K, 1273K, and 1473K—were considered for the external boundary of the TRISO particle. The comparison of particle fuel performance for different temperatures is shown in Figures 30 – 33. With the increase in temperature, the stresses in the TRISO layers are reduced. In the IPyC layer, the maximum radial stress decrease from ≈40 MPa at 1073 K to ≈32MPa at 1273 MPa and ≈20 MPa at 1473 K; the maximum tangential stress reduce from ≈240 MPa at 1073 K to ≈170 MPa at 1273 K and ≈120 MPa at 1473 K. In the SiC layer, the maximum radial stress decrease from ≈30 MPa at 1073 K to ≈20MPa at 1273 MPa and ≈10 MPa at 1473 K; the maximum tangential stress magnitude reduce from ≈400 MPa at 1073 K to ≈280 MPa at 1273 K and ≈200 MPa at 1473 K. This decrease in the stresses is due to the increases in the creep strain at the higher temperature, which relaxes the stresses. As the tensile stresses decrease, the failure probabilities for the PyC and SiC layers also decrease considerably. For the anisotropic case, failure probability of the IPyC layer decreases from 0.98 at 1073 K to 0.13 at 1273 K and 0.0067 at 1473 K, while for the isotropic case, the failure probability of the IPyC layer decreases from 0.78 at 1073 K to 0.074 at 1273 K and 0.0043 at 1473 K. For the anisotropic case, failure probability of the SiC layer decreases from 8.1×10^{-8} at 1073 K to 9.1×10^{-9} at 1273 K and 1.26×10^{-9} at 1473 K, while for the isotropic case, failure probability of the SiC layer decreases from 4.69×10^{-8} at 1073 K to 7.1×10^{-9} at 1273 K and 1.1×10^{-9} at 1473 K. It can be noted that in general, the differences in the stresses and failure probabilities for the isotropic and anisotropic cases are greater at lower temperature.

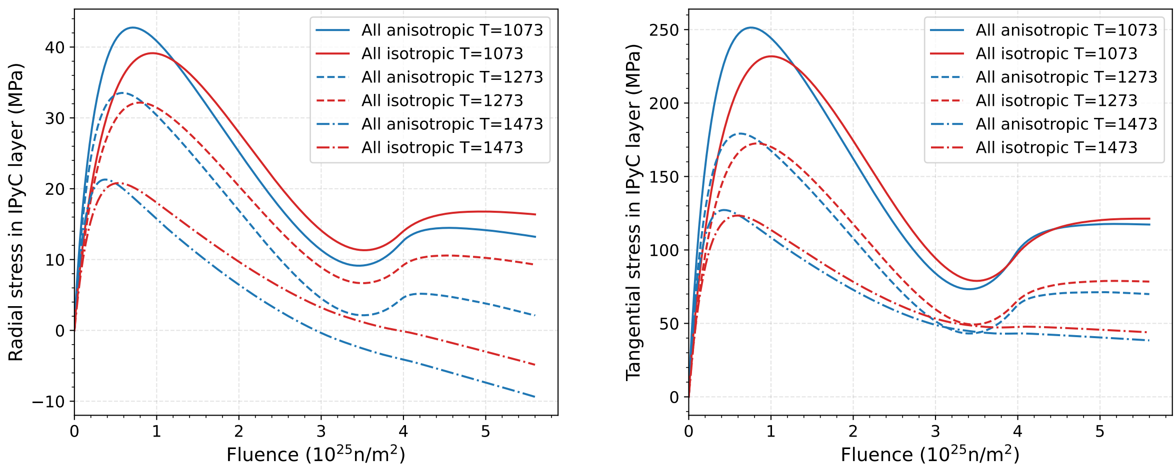

Figure 30. Variation of radial and tangential stresses with fluence in the IPyC layer of the TRISO particle for different temperatures (unit: Kelvin).

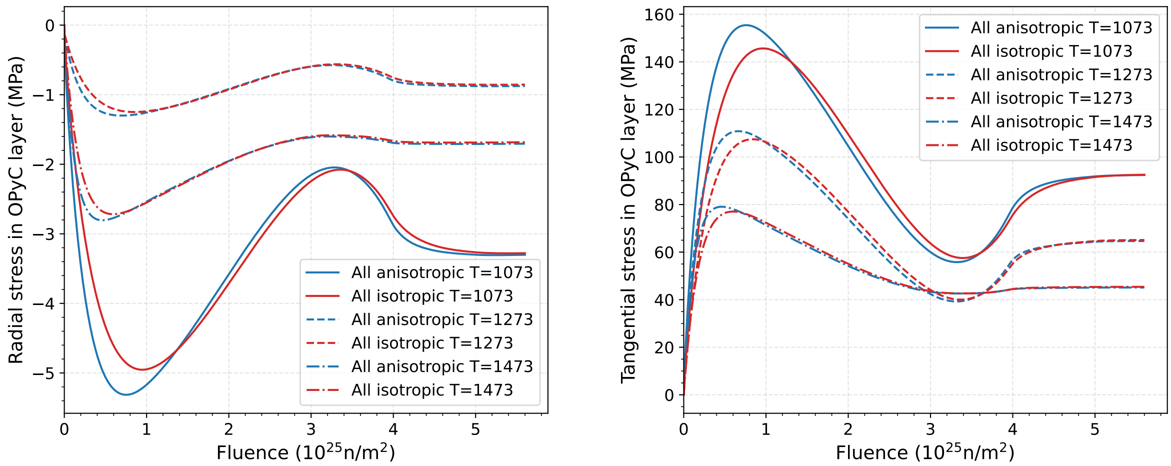

Figure 31. Variation of radial and tangential stresses with fluence in the OPyC layer of the TRISO particle for different temperatures (unit: Kelvin).

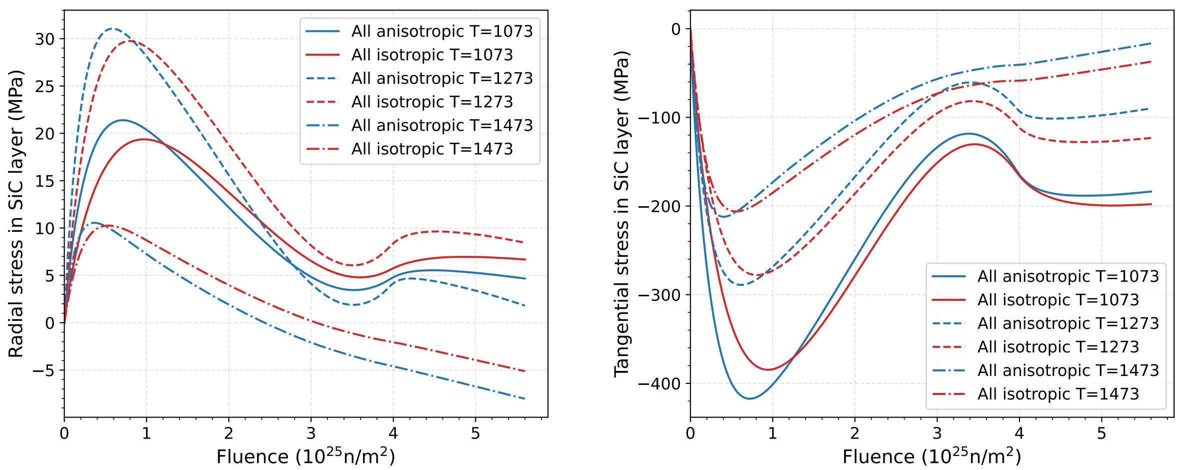

Figure 32. Variation of radial and tangential stresses with fluence in the SiC layer of the TRISO particle for different temperatures (unit: Kelvin).

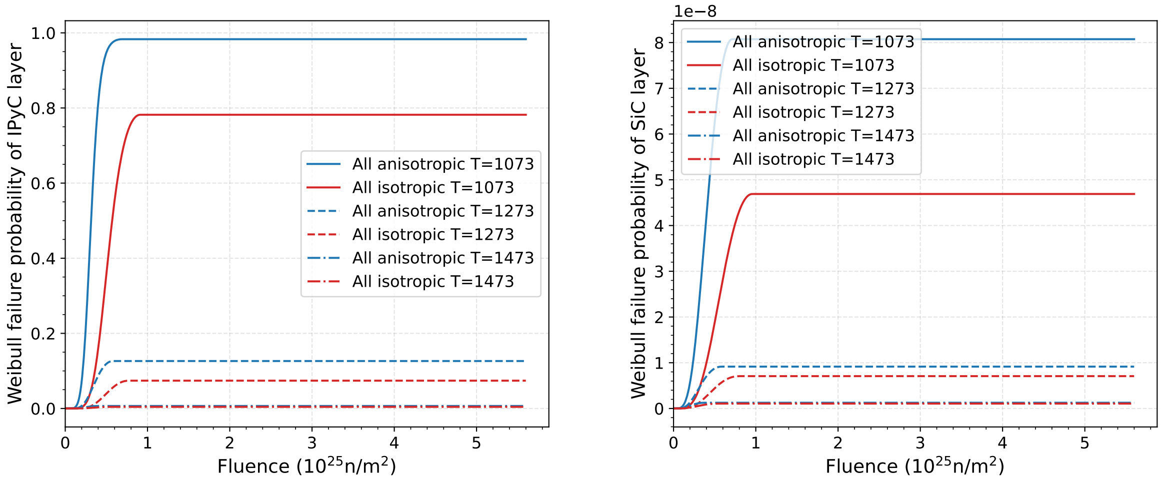

Figure 33. Variation of failure probability of the IPyC and SiC layers with fluence for different temperatures (unit: Kelvin).

4.7. Comparison with Legacy Models

This subsection presents how the stresses and failure probabilities based on the Evans models [29] compare with those based on the legacy models for elasticity and thermal behavior of PyC layers used in the PARFUME code [3, 40]. The details of the legacy models for PyC layers are given in Section 2.3. These legacy models assume different radial and tangential Young's moduli, and isotropic thermal conductivity. The comparison results are shown in Figures 34 – 37. In general, the maximum stress values obtained using the Evans models are comparable to those obtained using the legacy models, with the legacy models yielding slightly greater value of the stress magnitudes and failure probabilities.

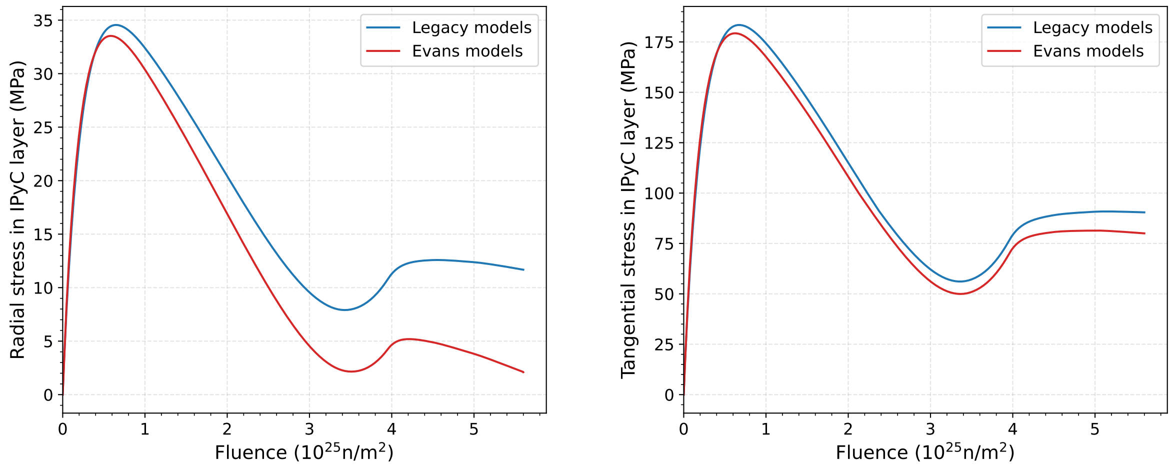

Figure 34. Comparison of the radial and tangential stresses in the IPyC layer using the legacy and Evans models.

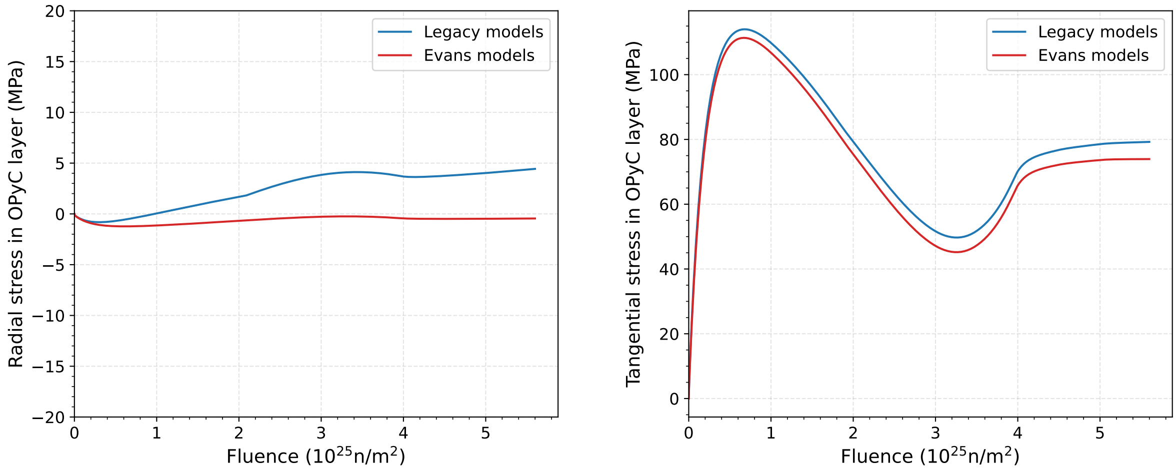

Figure 35. Comparison of the radial and tangential stresses in the OPyC layer using the legacy and Evans models.

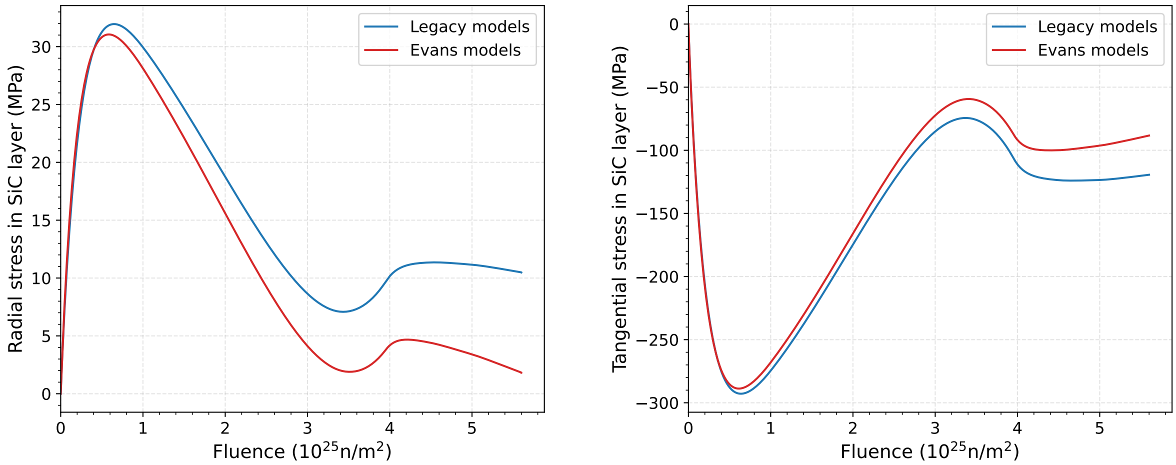

Figure 36. Comparison of the radial and tangential stresses in the SiC layer using the legacy and Evans models.

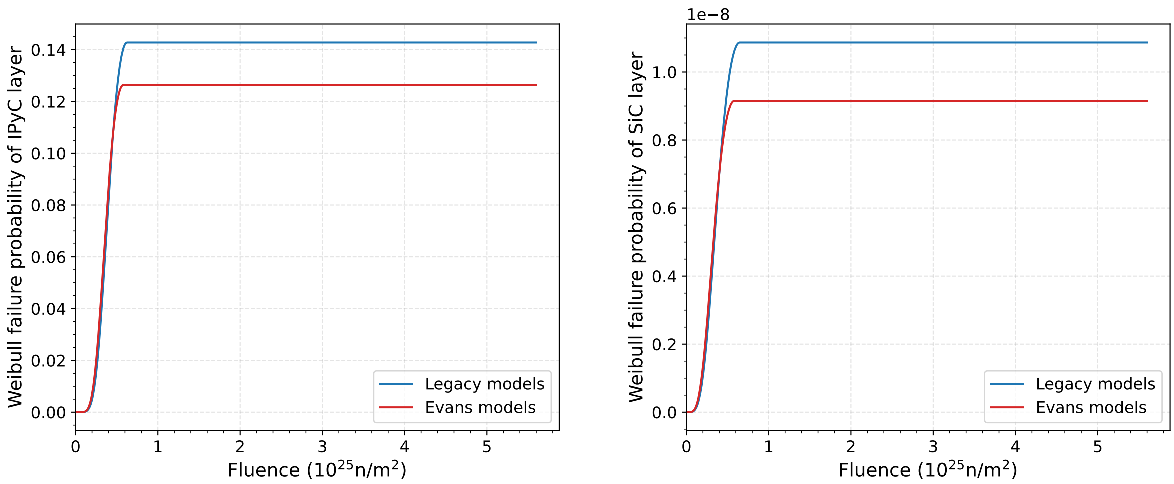

Figure 37. Comparison of the Weibull failure probability of (a) the IPyC layer and (b) the SiC layer using the legacy and Evans models.

5. Conclusion and Future Work

In the work presented, simulations were performed to assess TRISO fuel performance using the Evans models that account for anisotropic elasticity and thermal properties of the constituent layers of a TRISO particle. The computed stresses and failure probabilities were compared with the case with isotropic properties. The effect of anisotropic properties of individual layers of the TRISO particle is also assessed. A comparison of the predicted stresses and failure probability using the Evans models with those obtained based on the legacy models is also presented. The following conclusions can be drawn based on the results:

- The failure probability of a spherical TRISO particle with anisotropic properties is significantly higher from that of a spherical particle with isotropic properties.
- The maximum tensile stress reached in the TRISO particle layers and the corresponding failure probabilities are greater for the particle with anisotropic properties.
- The anisotropy in the thermal properties of buffer layer has greater impact on the stresses in the SiC layer compared to the anisotropy in the thermal properties of PyC layers.
- The geometry of a TRISO particle can strongly influence how the anisotropy in material properties of particle layers affect its fuel performance. The extent of the influence will likely depend on the smoothness in the layers' radii transition.
- With the rise in operating temperature between 800°C - 1200°C, the stresses and failure probability of a TRISO particle decreases. The influence of anisotropy on the stresses and failure probability is also more pronounced at lower temperatures.
- The stresses and failure probabilities of the TRISO particle predicted using the Evans models are comparable with those predicted using the legacy models for PyC.

It should be noted that the textures of the coating layers considered in this study are not representative of the textures of the fresh fuel used in the AGR program. So, the conclusions of this study does not indicate that the TRISO fuel is less safe. There has been lack of understanding of how to more accurately describe the effect of anisotropy in the structural and thermal properties of the coating layers may have on the TRISO fuel performance. This study aims just to fill in this knowledge gap using the fully tensorial description of anisotropy rather than simple scalar approximations like the Bacon anisotropy factor.

In this work, the texture (quantified using the BAF) was considered to be constant and independent of the neutron irradiation and temperature. In reality, temperature and irradiation change the texture, and it is expected that the texture increase with an increase in the neutron fluence. The data presented in Bokros et al. [39] shows that the irradiation-induced dimensional changes are anisotropic and strongly dependent on the irradiation, and the anisotropy increases with irradiation. Future work will incorporate the dependence of texture on the irradiation conditions.

Acknowledgments

This manuscript has been authored by Battelle Energy Alliance, LLC, under Contract No. DE-AC07-05ID14517 with the U.S. Department of Energy, with funding from the Nuclear Energy Advanced Modeling and Simulation (NEAMS) program. The U.S. Government retains and the publisher, by accepting the article for publication, acknowledges that the U.S. Government retains a nonexclusive, paid-up, irrevocable, worldwide license to publish or reproduce the published form of this manuscript, or allow others to do so, for U.S. Government purposes.

The authors are thankful to Dr. Adam Zabriskie and Dr. Lynn Munday for performing the internal technical review of this paper. This research made use of the resources of the High Performance Computing Center at Idaho National Laboratory, which is supported by the Office of Nuclear Energy of the U.S. Department of Energy and the Nuclear Science User Facilities under Contract No. DE-AC07-05ID14517.

Appendix

Legacy Models for Elaticity in TRISO Coating Layers

The radial and tangential Young's moduli, E_r and E_p, for the legacy model for PyC (models used in PARFUME code [3]) are expressed as:

$$E_r = 25.5(0.384 + 0.324 \times 10^{-3}\rho)(1.463 - 0.463BAF_0)(2.985 - 0.0662L_c)(1 + 0.23\phi)[1 + 0.00015(T - 20)] \quad (13)$$

$$E_p = 25.5(0.384 + 0.324 \times 10^{-3}\rho)(0.481 + 0.519BAF_0)(2.985 - 0.0662L_c)(1 + 0.23\phi)[1 + 0.00015(T - 20)] \quad (14)$$

where ρ (kg/m^3) is density, BAF_0 (= 1.05 dimensionless) is the as-fabricated anisotropy, L_c (= 30 Angstroms) is the crystallite diameter, ϕ (10^{25} n/m^2, E >0.18 MeV) is the fast neutron fluence, and T (°C) is the temperature. Poisson's ratios ν_{rp} and ν_p are assumed to have a constant value of 0.33, while Poisson's ratio ν_{pr} is calculated to be $\nu_{rp}E_p/E_r$.

For the legacy model, the thermal conductivity of the PyC layer is considered to be constant at 4.0 W/m-K [3]. The thermal conductivity (k) of the buffer layer for the legacy model is given in Eq. 15.

$$k = \frac{k_{init}k_{theo}(\rho_{theo} - \rho_{init})}{k_{theo}(\rho_{theo} - \rho) + k_{init}(\rho - \rho_{init})}, \quad (15)$$

where k_{init} (0.5 W/m-K) is the initial thermal conductivity of the layer [3] with an initial density (ρ_{init}) of 1000 kg/m^3. The theoretical density (ρ_{theo}) and thermal conductivity at theoretical density (k_{theo}) are set at 2250 kg/m^3 and 4.0 W/m-K, respectively.

Legacy Models for Thermal Properties of TRISO Coating Layers

The thermal conductivity of the SiC layer is described through Eq. 16 [41]:

$$k \text{ (W/m-K)} = \frac{1}{\frac{1}{k_{unirradiated}} + R_{irradiated}} \quad (16)$$

where $k_{unirradiated}$ is expressed as in Eq. 17.

$$k_{unirradiated} = \frac{1}{-0.0003 + 1.05 \times 10^{-5} T} \tag{17}$$

with T being the temperature (K). The increase in thermal resistance with irradiation $R_{irradiated}$ is expressed through Eq. 18.

$$R_{irradiated} = 0.00135 + 6.13 \epsilon_{irrad}^{vol} \tag{18}$$

where ϵ_{irrad}^{vol} is the volumetric swelling strain due to irradiation.

The specific heat capacities for PyC and buffer were both set at 720 J/kg-K. The specific heat capacity for the SiC according to the Snead model [41] described in Eq. 19.

$$C_p = 925.65 + 0.3772T - 7.9259 \times 10^{-5} T^2 - \frac{3.1946 \times 10^7}{T^2} \tag{19}$$

where T is the temperature (K).

Irradiation Swelling in TRISO Coating Layers

The expression for linear irradiation-induced strain for the buffer is expressed through Eq. 20.

$$\epsilon_{irrad} = \frac{\epsilon_{iso}(\rho)}{\epsilon_{iso}(\rho = 1.96 \text{ g/cm}^3)} \left(A_1 \gamma + A_2 \gamma^2 + A_3 \gamma^3 + A_4 \gamma^4 \right) \tag{20}$$

where A_i are the constants given in Table 6 for three different temperatures, γ (10^{25} n/m^2, E>0.18 MeV) is the fast neutron fluence, and ϵ_{iso} is the isotropic strain with its values for different densities given in Table 7. For calculating the strain at a particular temperature, linear interpolation or extrapolation is performed.

Table 6. Coefficients for irradiation swelling in buffer ([3, 25])

Temperature (°C)	A_1	A_2	A_3	A_4
1350	-1.42840	-0.19563	0.18991	-0.02591
1032	-1.52390	0.13048	0.06299	-0.01072
600	-1.24080	0.00175	0.08533	-0.01253

Table 7. Isotropic strain at irradiation temperature of 1100°C and fast fluence of 3.7x10^{25} n/m^2 (E>0.18 MeV) ([25])

ρ (g/cm^3)	1.0	1.2	1.4	1.5	1.6	1.8	1.9	1.96	2.0
ϵ_{iso} (%)	-16.15	-13.11	-9.98	-8.93	-6.97	-4.42	-3.41	-2.75	-2.33

The model used for the irradiation-swelling of the PyC layers is very similar to that for the buffer layer. Details about this model can be found in reference [3]. The irradiation swelling for the SiC layer was calculated using the Katoh model [41, 42] as given in Eq. 21.

$$\epsilon_{irrad}^{vol} = \epsilon_{saturated}\left[1 - \exp\left(-\frac{\gamma}{\gamma_c}\right)\right]^{2/3} \tag{21}$$

where ϵ_s is the saturated swelling strain (volumetric), γ is the dose in dpa, and γ_c is the characteristic dose in dpa for swelling saturation. The saturated swelling and characteristic dose are polynomial functions of temperature T as:

$$\epsilon_{saturated} = 5.8366 \times 10^{-2} - 1.0089 \times 10^{-4} T + 6.9368 \times 10^{-8} T^2 - 1.8152 \times 10^{-11} T^3 \tag{22}$$

$$\gamma_c = -0.57533 + 3.3342 \times 10^{-3} T - 5.3970 \times 10^{-6} T^2 + 2.9754 \times 10^{-9} T^3 \tag{23}$$

Thermal Expansion of TRISO Coating Layers

The radial and tangential coefficients (α_r and α_t) of thermal expansion for PyC layers as used in PARFUME code [3] are given in Eq. 24 and Eq. 25, respectively in units of 10^{-6}/°C.

$$\alpha_r = \left(30 - \frac{75}{2 + BAF}\right)\left(1 + 0.11\left[\frac{T - 673}{700}\right]\right) \tag{24}$$

$$\alpha_t = \left(\frac{36}{(2 + BAF)^2} + 1\right)\left(1 + 0.11\left[\frac{T - 673}{700}\right]\right) \tag{25}$$

where T is temperature (K) and BAF is the Bacon anisotropy factor (1.0 for the isotropy case and 1.05 for the anisotropy case in this analysis). The thermal expansion model used for the buffer is described in Eq. 26 in units of 10^{-6}/°C.

$$\alpha = 5\left(1 + 0.11\frac{T - 400}{700}\right) \tag{26}$$

where T is temperature (°C). The thermal expansion coefficient for SiC was set at 4.9 $\times 10^{-6}$ (1/K).

Creep of TRISO Coating Layers

The creep strain (ϵ_c) for the PyC is computed using the model presented in references [43] and [44], and is given in Eq. 27.

$$\dot{\epsilon}_c = K\sigma\dot{\gamma} \tag{27}$$

where σ is the stress, γ is the fast neutron fluence, and K is the creep coefficient given in Eq. 28 as:

$$K = K_o[1 + 2.38(1.9 - \rho)]M_{\text{irr,creep}} \tag{28}$$

where ρ is the density given in g/cm^3 and $M_{\text{irr,creep}}$ is 2.0. The steady state creep coefficient, K_o, is given by reference

[3] as Eq. 29:

$$K_o = 2.193 \times 10^{-29} - 4.85 \times 10^{-32} T + 4.0147 \times 10^{-35} T^2 \tag{29}$$

where T is temperature (°C). The creep strain for the buffer is calculated using the same expression (Eq. 27), with the creep coefficient K as defined in Eq. 30 [3].

$$K = A(1 + 2.38[1.9 - \rho])(2.193 \times 10^{-29} - 4.85 \times 10^{-32} T + 4.0147 \times 10^{-35} T^2) \tag{30}$$

where A is a creep scale factor to adjust the magnitude of creep strain in order to account for the uncertainty in the creep data. The value of $A = 2.0$ allows a fit with the data from the New Production Reactor Program and is used as such. The ρ is the density in g/cm^3 and T is the temperature (°C).

References

[1] S. D. Rubin, Triso-coated particle fuel phenomenon identification and ranking tables (pirts) for fission product transport due to manufacturing, operations and accidents, Tech. Rep. IAEA-TECDOC-CD–1614 (Apr 2009).

[2] J. Hales, R. Williamson, S. Novascone, D. Perez, B. Spencer, G. Pastore, Multidimensional multiphysics simulation of triso particle fuel, Journal of Nuclear Materials 443 (1-3) (2013) 531–543.

[3] G. K. Miller, D. A. Petti, J. T. Maki, D. L. Knudson, W. F. Skerjanc, PARFUME theory and model basis report, Tech. Rep. INL/EXT-08-14497 (Rev.1), Idaho National Laboratory, Idaho Falls, ID (United States) (9 2018). `doi:10.2172/1471713`.
URL `https://www.osti.gov/biblio/1471713-parfume-theory-model-basis-report`

[4] J. T. Keeley, B. L. Tomlin, W. C. Richardson, C. Barnes, D. Marshall, Development of a continuous cvd process for triso coating of agr fuel, in: High Temperature Reactor Technology, Vol. 48548, 2008, pp. 1–6.

[5] M. Liu, R. Liu, B. Liu, Y. Shao, Preparation of the coated nuclear fuel particle using the fluidized bed-chemical vapor deposition (fb-cvd) method, Procedia engineering 102 (2015) 1890–1895.

[6] E. López-Honorato, P. Meadows, P. Xiao, Fluidized bed chemical vapor deposition of pyrolytic carbon–i. effect of deposition conditions on microstructure, Carbon 47 (2) (2009) 396–410.

[7] E. L. Honorato, P. Xiao, G. Marsh, T. Abram, Fluidised bed chemical vapour deposition of pyrolytic carbon, Ceramics in Nuclear and Alternative Energy Applications: Ceramic Engineering and Science Proceedings 27 (2007) 101–114.

[8] N. Yoshikawa, S. Taniguchi, A. Kikuchi, Morphology and texture of chemical-vapour-deposited tin films, MRS Online Proceedings Library (OPL) 472.

[9] R. Clausing, L. Heatherly, L. Horton, E. Specht, G. Begun, Z. Wang, Textures and morphologies of chemical vapor deposited (cvd) diamond, Diamond and Related Materials 1 (5-6) (1992) 411–415.

[10] H. Zhang, E. López-Honorato, P. Xiao, Fluidized bed chemical vapor deposition of pyrolytic carbon-iii. relationship between microstructure and mechanical properties, Carbon 91 (2015) 346–357.

[11] P. Meadows, E. López-Honorato, P. Xiao, Fluidized bed chemical vapor deposition of pyrolytic carbon–ii. effect of deposition conditions on anisotropy, Carbon 47 (1) (2009) 251–262.

[12] G. E. Jellison Jr, J. D. Hunn, R. A. Lowden, Optical characterization of tristructural isotropic fuel particle cross-sections using generalized ellipsometry, Journal of nuclear materials 352 (1-3) (2006) 6–12.

[13] E. Bortchagovsky, B. Reznik, D. Gerthsen, A. Pfrang, T. Schimmel, Optical properties of pyrolytic carbon deposits deduced from measurements of the extinction angle by polarized light microscopy, Carbon 12 (41) (2003) 2430–2433.

[14] A. Pfrang, T. Schimmel, Quantitative analysis of pyrolytic carbon films by polarized light microscopy, Surface and Interface Analysis: An

International Journal devoted to the development and application of techniques for the analysis of surfaces, interfaces and thin films 36 (2) (2004) 184–188.

[15] L. Tan, T. R. Allen, J. D. Hunn, J. H. Miller, Ebsd for microstructure and property characterization of the sic-coating in triso fuel particles, Journal of Nuclear Materials 372 (2-3) (2008) 400–404.

[16] D. Helary, O. Dugne, X. Bourrat, P.-H. Jouneau, F. Cellier, Ebsd investigation of sic for htr fuel particles, Journal of nuclear materials 350 (3) (2006) 332–335.

[17] B. Reznik, K. Hüttinger, On the terminology for pyrolytic carbon, Carbon 40 (4) (2002) 621–624.

[18] E. López-Honorato, P. Meadows, P. Xiao, G. Marsh, T. Abram, Structure and mechanical properties of pyrolytic carbon produced by fluidized bed chemical vapor deposition, Nuclear Engineering and Design 238 (11) (2008) 3121–3128.

[19] E. López-Honorato, P. Meadows, J. Tan, Y. Xiang, P. Xiao, Deposition of triso particles with superhard sic coatings and the characterization of anisotropy by raman spectroscopy, Journal of engineering for gas turbines and power 131 (4).

[20] X. Zhao, F. Yang, H. Zhang, P. Xiao, Nondestructive evaluation of high-temperature elastic modulus of 3c-sic using raman scattering, Journal of Raman Spectroscopy 43 (7) (2012) 945–948.

[21] D. W. Marshall, Agr-5/6/7 fuel fabrication report, Tech. rep., Idaho National Lab.(INL), Idaho Falls, ID (United States) (2019).

[22] J. Phillips, C. Barnes, J. Hunn, Fabrication and comparison of fuels for advanced gas reactor irradiation tests, Tech. rep., Idaho National Lab.(INL), Idaho Falls, ID (United States) (2010).

[23] J. D. Hunn, R. A. Lowden, J. H. Miller, B. C. Jolly, M. P. Trammell, A. K. Kercher, F. C. Montgomery, C. M. Silva, Fabrication and characterization of driver-fuel particles, designed-to-fail fuel particles, and fuel compacts for the us agr-3/4 irradiation test, Nuclear Engineering and Design 271 (2014) 123–130.

[24] S. Feng, Y. Yang, L. Li, D. Zhang, X. Yang, S. Bai, H. Xia, L. Yan, P. Huai, X. Zhou, Effect of ar+ ion irradiation on the microstructure of pyrolytic carbon, Journal of Applied Physics 117 (11) (2015) 115101.

[25] F. Ho, et al., Material models of pyrocarbon and pyrolytic silicon carbide, CEGA-002820, Rev 1.

[26] D. G. Martin, Considerations pertaining to the achievement of high burn-ups in htr fuel, Nuclear engineering and design 213 (2-3) (2002) 241–258.

[27] P. A. Demkowicz, J. Hunn, D. W. Marshall, Advanced gas reactor fuel specification technical bases, Tech. rep., Idaho National Laboratory (INL), Idaho Falls, ID (United States) (2023).

[28] D. Stevens, Round robin optical measurements of preferred orientation in nearly isotropic pyrocarbon, Tech. rep., General Atomics, San Diego, CA (United States) (1979).

[29] J. A. Evans, R. A. Lebensohn, J. R. Harter, K. D. Weaver, Anisotropic temperature-dependent elastic constants and thermal conductivities of triso particle coatings, Journal of Nuclear Materials 565 (2022) 153718.

[30] A. Toptan, W. Jiang, G. Singh, S. L. Dhulipala, Y. Che, J. D. Hales, S. R. Novascone, Assessment and improvement of fission product transport predictions of particle fuel in bison, Tech. Rep. INL/RPT-22-69706, Idaho National Lab.(INL), Idaho Falls, ID (United States) (2022).

[31] R. L. Williamson, J. D. Hales, S. R. Novascone, G. Pastore, K. A. Gamble, B. W. Spencer, W. Jiang, S. A. Pitts, A. Casagranda, D. Schwen, A. X. Zabriskie, A. Toptan, R. Gardner, C. Matthews, W. Liu, H. Chen, BISON: A flexible code for advanced simulation of the performance of multiple nuclear fuel forms, Nuclear Technology 207 (7) (2021) 954–980. doi:10.1080/00295450.2020.1836940.

[32] J. D. Hunn, T. W. Savage, G. Silva, Agr-2 fuel compact pre-irradiation characterization summary report, Tech. rep., Oak Ridge National Lab.(ORNL), Oak Ridge, TN (United States) (2010).

[33] P. A. Demkowicz, B. P. Collin, D. A. Petti, G. L. Hawkes, J. W. Sterbentz, B. T. Pham, D. M. Scates, D. E. Stacey, Results of the agr-2 triso fuel performance demonstration irradiation experiment in the advanced test reactor, Annals of Nuclear Energy 150 (2021) 107833.

[34] P. A. Demkowicz, Triso fuel part i: Background, fabrication, and irradiation performance, Tech. Rep. INL/MIS-21-62429-Rev.0, Idaho National Lab.(INL), Idaho Falls, ID (United States) (2021).

[35] W. Jiang, J. D. Hales, B. W. Spencer, B. P. Collin, A. E. Slaughter, S. R. Novascone, A. Toptan, K. A. Gamble, R. Gardner, Triso particle fuel

performance and failure analysis with bison, Journal of Nuclear Materials 548 (2021) 152795.

[36] B. P. Collin, Generation iv benchmarking of triso fuel performance models under accident conditions: Modeling input data, Tech. Rep. INL/EXT-20-60147-Rev.0, Idaho National Lab.(INL), Idaho Falls, ID (United States) (2014).

[37] E. López-Honorato, J. Boshoven, P. Meadows, D. Manara, P. Guillermier, S. Jühe, P. Xiao, J. Somers, Characterisation of the anisotropy of pyrolytic carbon coatings and the graphite matrix in fuel compacts by two modulator generalised ellipsometry and selected area electron diffraction, Carbon 50 (2) (2012) 680–688.

[38] G. E. Jellison Jr, J. D. Hunn, Optical anisotropy measurements of triso nuclear fuel particle cross-sections: The method, Journal of nuclear materials 372 (1) (2008) 36–44.

[39] J. Bokros, R. Price, Radiation-induced dimensional changes in pyrolytic carbons deposited in a fluidized bed, Carbon 4 (3) (1966) 441–454.

[40] W. F. Skerjanc, J. T. Maki, B. P. Collin, D. A. Petti, Evaluation of design parameters for triso-coated fuel particles to establish manufacturing critical limits using parfume, Journal of Nuclear Materials 469 (2016) 99–105.

[41] L. L. Snead, T. Nozawa, Y. Katoh, T.-S. Byun, S. Kondo, D. A. Petti, Handbook of sic properties for fuel performance modeling, Journal of nuclear materials 371 (1-3) (2007) 329–377.

[42] Y. Katoh, K. Ozawa, C. Shih, T. Nozawa, R. J. Shinavski, A. Hasegawa, L. L. Snead, Continuous sic fiber, cvi sic matrix composites for nuclear applications: Properties and irradiation effects, Journal of Nuclear Materials 448 (1-3) (2014) 448–476.

[43] D. Petti, P. Martin, M. Phelip, R. Ballinger, Development of improved models and designs for coated-particle gas reactor fuels–final report under the international nuclear energy research initiative (i-neri), Tech. Rep. INEEL/EXT-05-02615, Idaho National Lab.(INL), Idaho Falls, ID (United States); Centre d'Etude … (2004).

[44] J. J. Powers, B. D. Wirth, A review of triso fuel performance models, Journal of Nuclear Materials 405 (1) (2010) 74–82.